UNIVERSITÀ DEGLI STUDI DI PADOVA

Dipartimento di Fisica e Astronomia "Galileo Galilei"

Master Degree in Astrophysics and Cosmology

Final Dissertation

Multiple populations among very low-mass stars in NGC 288

Thesis Supervisor:

Prof. Antonino P. Milone

Candidate:

Emanuele Bortolan

Thesis Co-Supervisor:

Dr. Emanuele Dondoglio

ACCADEMIC YEAR 2021/2022

Abstract

Globular Clusters (GCs) are among the oldest objects in the Universe. Nearly all GCs host two main stellar groups of stars, a first population (1P) with a chemical composition similar to halo field stars with similar metallicity, and the second population (2P) of stars enriched in He, N, Na, and Al and depleted in O and C.

The astronomers have proposed two main scenarios to explain the formation of multiple populations in GCs, namely the single- and the multiple-generation scenarios. Each of them has major implications in Cosmology, Galactic Archaeology, and stellar evolutionary models.

For these reasons, the knowledge of GCs' formation and evolution is crucial to shed light on the formation and evolution of the Galaxy. Nowadays, most of the studies on multiple populations are focused on stars more massive than $\sim 0.5-0.6\ M_\odot$, whereas the Very Low-Mass (VLM) regime is almost unexplored.

Nonetheless, VLM stars would provide crucial information to constrain the formation scenarios. Indeed, the different scenarios predict different chemical abundances for 2P stars with different masses. In the single-generation scenario, 2P stars with different masses also have different light-element abundance, while the multiple-generation scenarios predict that all 2P stars share the same chemical composition.

In this research, I use Hubble Space Telescope images to investigate the GC NGC 288 and characterize, for the first time, its multiple stellar populations among VLM stars. To this, I derive the m_{F160W} versus $m_{F110W} - m_{F160W}$ Color-Magnitude Diagram (CMD), which is a very efficient tool to disentangle multiple stellar populations below the main sequence (MS) knee.

As expected, I detected two distinct MSs of M-dwarfs and I showed that the MS split is due to stellar populations with different oxygen abundances. I associated the blue and red stellar sequences with 1P and 2P stars, respectively.

Based on isochrones and synthetic spectra with appropriate chemical compositions that I computed for this work, I derived the colors of 1P and 2P stars corresponding to different abundances of He, C, N, and O. The comparison between these isochrones and the observed CMD allowed me to infer the oxygen abundance of 1P and 2P stars.

I found that 2P M-dwarfs are enhanced in oxygen by $\Delta\,[\mathrm{O/Fe}] = 0.33 \pm 0.03$ dex with respect to 1P VLM stars. Such oxygen variation is comparable with that derived from high-resolution spectroscopy of red-giant branch stars. The finding that the chemical composition of 2P stars does not depend on stellar mass is consistent with the predictions of the multiple-generation scenarios.

i

Contents

Chapter 1

Globular Clusters: a multiple populations phenomenon

Globular Clusters (GCs) are one of the oldest objects in the Universe, therefore, through their study, we can obtain useful information about the first stages of the Universe and how the first structures formed. Moreover, most of the Galactic GCs (around 150 GCs) formed at Redshift $z \gtrsim 3$ (Dotter et al 2010), and they should have been more massive compared to how they are nowadays (see Section 1.2.1). At that epoch, only a tiny fraction of the Galaxy's stellar mass ($\sim 6\%$) was formed (Madau & Dickinson 2014). As a consequence, they should have played a pivotal role in the assembly of the Milky Way and its first evolutionary stages and they could have also contributed to the re-ionization of the Universe. For all these reasons, the knowledge of GCs' formation and evolution is a crucial tool shed light on how the Universe works.

Until the end of the XX century, astronomers thought that GCs were prototypes of Simple Stellar Populations (SSPs), which are stellar populations that formed in a single burst of star formation from a chemical homogeneous gas cloud. A SSP can be easily described by three main parameters: age, distance, and chemical composition of the pristine gas cloud. A good example of a GC that resembles an SSP is NGC 6397, one of the closest GCs, whose Color Magnitude Diagram (CMD) is shown on the left panel in Figure 1.1. On the right panel, a model of an SSP is overplotted and we can see that it fits quite well the Main Sequence (MS) of NGC 6397, suggesting that the GC represents an SSP.

1.1 Observational evidences for multiple populations

The hint of the possible presence of multiple stellar populations (MSPs) arose initially through the analysis of the stellar spectra within GCs. Indeed, it was found star-to-star abundance variations, in particular among light elements (Cohen 1978, Norris et al 1981, Norris 1981, Norris & Freeman 1982, Smith & Penny 1989.). However, these observations were based on a limited number of
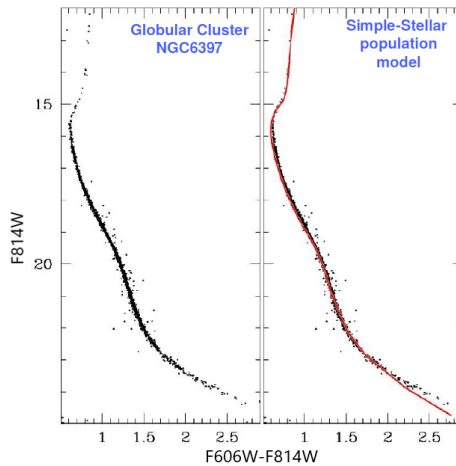
Figure 1.1: Left panel shows the CMD of NGC 6397, in the right panel it is overlapped an SSP model, which fits quite well. (Image taken from Prof. Milone's lecture notes)

giant stars, so that it was still unclear if those anomalous stars were part of a chemically-different stellar population or if their presence was due to evolutionary reasons (see Kraft 1994 for a review).

Another way to investigate GCs is using photometry, which has improved significantly since the Hubble Space Telescope (HST) became operational. Indeed, with the combination of an appropriate set of filters that are sensitive to different chemical abundances, photometry can be equivalent to very low-resolution spectroscopy, with the advantages of being able to observe wider regions of the sky and sampling stellar populations composed of several thousand stars. The synergy between these two techniques, photometry and spectroscopy, has uncovered without any doubt the presence of multiple stellar populations within almost all GCs observed so far. Among all observations, there are three main pieces of observational evidence that have helped astronomers to abandon the idea of GCs as prototypes of SSP in favor of the MSP scenario.

The first evidence is the chemical composition of stars within a GC. Indeed, star-to-star chemical variations were observed in elements involved in hot hydrogen burning and in p-capture processes, e.g. C, N, O, Na, Al, and in some GCs also in Mg, Si, and K. These variations are not arbitrary but they follow well-known patterns, such as O-Na, C-N and Mg-Al anti-correlations or Na-N, C-O and Si-Al correlations (e.g. Carretta et al. 2009). The left panel in Figure 1.2 displays the O-Na anti-correlation found by Carretta et al. (2009) by studying the spectra of almost 2000 stars in 19 different GCs. The right panel instead shows the C-N anti-correlation found by Cohen et al. (2002) analyzing Sub Giant Branch (SGB) stars in M5. Originally, these chemical inhomogeneities were thought to be caused by evolutionary mixing, considering that stellar evolution may contribute to explaining the observed N-C anti-correlation in evolved Red Giant Branch (RGB) stars (Denisenkov & Denisenkova 1990). However, the detection of this phenomenon also in non-evolved stars in the MS or slightly evolved stars in the MS Turn-Off (MSTO) (Briley et al. 2004) ruled out this scenario, since in these stars convective regions are almost absent and the mixing cannot reproduce these chemical patterns.
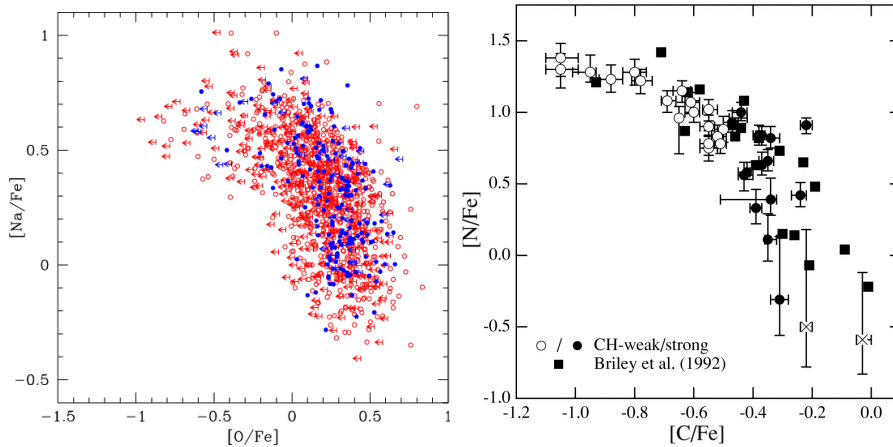
Figure 1.2: Left panel shows the Na-O anti-correlation found by Carretta et al. 2009 studying the spectra of 1958 stars in 19 different GCs obtained with the Very Large Telescope. Spectra obtained with the GIRAFFE and UVES spectrographs are shown as red and blue circles, respectively. The right panel, instead, shows the N-C anti-correlation found by Cohen et al. 2002 in SGB stars in M5. Black and white circles represent stars with strong or weak CH absorption bands, respectively, whereas black squares represent data from Briley et al. (1992).

Another piece of evidence is the so-called *second-parameter problem* of the Horizontal Branch (HB) (Sandage et al. 1967; Catelan 2009). It was thought that the only parameter that determines the morphology of the HB was metallicity. However, with the increase of observational data, together with the improvement of photometry, several GCs with the same metallicity but with a different HB morphology were found, some of them redder and others bluer, suggesting the presence of other parameters that alter the HB morphology.

The third main observational fact that challenges the SSP scenario is the presence of multiple sequences in the CMD of almost all GCs. Thanks to the photometry improvement in the last few decades, there was increasing evidence of broad or even split sequences into the different evolutionary phases in the CMD, from the MS (Milone et al. 2012a, Milone et al. 2012b) up to the Asymptotic-Giant Branch (AGB) (Lagioia et al. 2021) including the Red Giant Branch and the HB (Dondoglio et al. 2021) and even in the White Dwarf Cooling Sequence. These sequences are not just present separately in the different parts of the CMD but they can be followed continuously along with all evolutionary phases, suggesting the possible presence of MSPs (see the right panel in Figure 1.3 A few examples that well represent the complexity of MSPs phenomenon in GCs are NGC 7089 (M2), namely NGC 2808, and ω *Centauri* (NGC 5139), shown in figure 1.3. From the comparison between these CMD and the one in Figure 1.1 we can clearly see the presence of multiple sequences and the broadening of the MS and the RGB suggesting the presence of MSPs. In particular, the last two GCs, NGC 2808 and ω *Centauri*, were the first GCs that challenged seriously the SSP scenario of GC, since they are characterized by extreme chemical variations that produce well-separated sequences in their CMD.
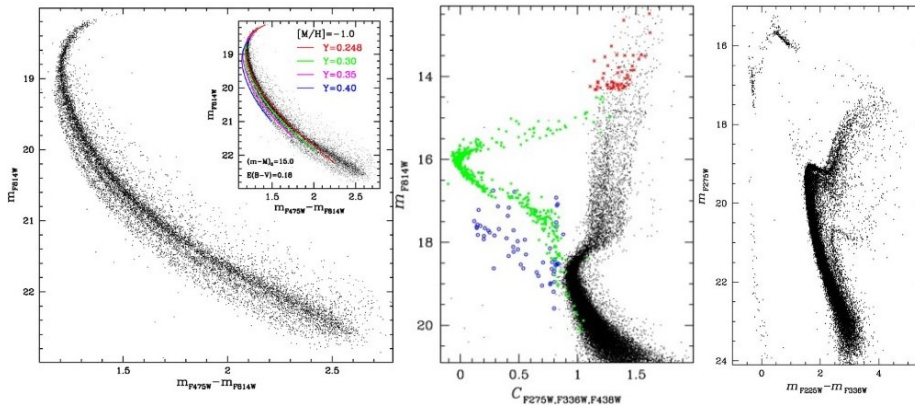
Figure 1.3: *Left panel*: CMD of NGC 2808, where several stellar sequences can be seen. The box in the upper left shows the same CMD with five isochrones superimposed to fit the different stellar populations. *Central panel*: the CMD of M2, with at least three different stellar tracks along the RGB. The different colors, represent AGB stars (red dots), HB stars (green dots), and Blue Struggles (blue dots) analyzed by Milone et al. (2014). *Right panel*: the CMD of ω Centauri where the different stellar populations can be seen from the bottom of the MS to the top of the RGB (left image from Piotto et al. 2007; central image from Milone et al. 2014; right image from Bellini et al. 2010).

After the discovery of these MSPs, astronomers developed new observational tools and approaches to maximize the separation between the different stellar populations, in order to get new information on their origin. Some of the most effective photometry-based approaches involve:

- *Wide-band UV photometry*. Marino et al. 2008 have demonstrated, studying M4, that wide-band ground-based photometry allows to separate efficiently different stellar populations, in particular using CMDs made with U-band filters. Indeed, stellar populations with a different abundance of C, Na, O, and S are arranged in distinct RGB sequences in a U versus U-B CMD, because each filter is sensitive to different bands, e.g. NH and CN molecular bands are included in the U filter whereas CH bands are included in the B filter.

- *Wide color baseline*. Stars with different He abundance have different effective temperatures, but the same luminosity. For this reason, He-rich stars are usually bluer in color than He-poor stars. To separate stellar populations with different He abundance, wide color baselines, as $m_{\mathrm{F275W}} - m_{\mathrm{F814W}}$, are usually employed because they are very sensitive to He variations, up to $\Delta Y = 0.01$. The most striking example comes from NGC2808, in which its large He variations produce three well-separated MSs (Piotto et al. 2007, Milone et al. 2012), as shown in the left panel in Figure 1.3.

- *Near-IR photometry*. IR photometry is very efficient to detect MSPs in very low-mass stars ($M \lesssim 0.4\ M_\odot$). The two main filters used for this purpose are the F110W and F160W of the WFC3/NIR camera onboard

4

HST. The F160W filter is very sensible to molecules that contain oxygen whereas the F110W filter is poorly affected by oxygen abundance. For that, the F110W-F160W color is effective in spotting chemical differences among these stars (e.g. Milone et al. 2012, 2014, 2017, 2019, Dondoglio et al. 2022). The NIR photometry will be discussed in details in Section 1.3.1.

- *Chromosome map (ChM).* Milone et al. (2015) have developed a pseudo-two-color diagram to efficiently disentangle different stellar populations. In this diagram, the stellar tracks present in the MS, RGB or AGB are verticalized in both dimensions, which is the main difference with respect to a simple two-color diagram. In doing so, considering that the colors used to build the ChM are sensitive to specific chemical abundances, the stellar populations are clustered in specific regions on this diagram depending on their chemical composition. The most common ChM exploits the $m_{\mathrm{F275W}} - m_{\mathrm{F814W}}$ color and the $C_{\mathrm{F275W,F336W,F814W}}$ pseudo-color, and it is most sensitive to He, C, N, and O variations (see also Milone et al. 2017 for details).

Thanks to these techniques two main stellar populations were found in almost all GCs: those stars with galactic-halo-field-like chemical composition, dubbed as first population (1P), and those with higher abundance of He, N, Na, and Al and depleted in C and O, dubbed second population (2P).

1.2 Formation scenarios

Since the discovery of these multiple populations phenomenon, astronomers have developed several possible scenarios trying to explain their origin. In particular, all the possible formation scenarios must explain the GC properties observed so far:

- *Light elements.* 2P stars are enhanced N, Na, and Al but depleted in C and O compared to 1P stars. In some clusters, variations in Mg and Si are also observed. Moreover, there are specific patterns among these elements, such as Na-O and C-N anti-correlations and Na-N and C-O correlations (see Figure 1.2). These chemical patterns are distinctive results from CNO-cycling and p-capture processes at high temperatures.

- *2P specificity.* The chemical composition mentioned in the previous point is a key feature of GCs considering the fact that stars with this chemical composition are found almost only in GCs and stars with this composition present outside GCs are considered generated within them and then stripped away or lost through tidal interactions (Vesperini et al. 2010). This unique feature suggests that the environment of GCs is necessary to form the chemical patterns found in 2P stars. For this reason, a formation scenario must account for the chemical composition of 2P stars and, at the same time, the rarity of these stars outside GCs.

- *Variety.* Although all GCs host MSPs, there are no two GCs that are exactly the same, i.e. each GC features a distinctive pattern of multiple populations, with a particular chemical composition. The formation scenario, therefore, has to explain the large cluster-to-cluster differences.

- *Predominance of 2P.* From observations, it has been seen that the stars 2P are the dominant component in almost all clusters with respect to 1P stars. Indeed, on average, the 1P stars contribute to $\sim 30 - 40\%$ to the total star mass within a GC, whereas 2P stars contribute to almost $\sim 60 - 70\%$.

- *Metallicity.* In almost all GCs, 1P and 2P stars share approximately the same metallicity $[Fe/H]$, within $\sim 0.1\ dex$. Given the fact that iron is mainly produced through core collapse Supernovae (SNe), the constancy of metallicity between the two populations indicates that the 2P stars have experienced limited contamination from SN ejecta.

- *He abundance.* Helium abundance is quite difficult to estimate through spectroscopy because stars colder than HB stars ($T_{\text{eff}} \lesssim 8000\ K$) do not have helium lines that are strong enough to be detected in the optical range, while hotter stars ($T_{\text{eff}} \gtrsim 11\,500\ K$) are affected by helium settling, hence the He content in their atmosphere is not indicative of their intrinsic He abundance. However, with multi-band photometry astronomers are able to constrain the He abundance of GC stars. In particular, we can obtain an estimate of the measure of He abundance by comparing the observed colors of different stellar populations with colors obtained through synthetic spectra with specific chemical abundances. From this technique, it is found that the difference in He abundance between 1P and 2P stars is, on average, $\Delta Y_{\text{1P}-\text{2P}} \sim 0.01$ in He mass fraction (Lagioia et al 2019, Milone et al. 2018). However, there are some GCs that show higher $\Delta Y_{\text{1P}-\text{2P}}$, with the highest $\Delta Y_{\text{1P}-\text{2P}} \sim 0.18$ found in NGC2419 (Zennaro et al. 2019).

- *Discreteness.* This is an important characteristic of MSPs. Indeed, within a GC, the different stellar populations can be split into discrete sequences in the CMD and appropriated two-color diagrams.

The majority of the formation scenarios can be summarized into two main groups: *Multiple Generations* and *Single Generation* scenarios.

1.2.1   Multiple Generations scenarios

According to Multiple Generations scenarios, different stellar populations correspond to different generations of stars. The 1P formed from a first burst of star formation within a homogeneous gas cloud composed of pristine material which resembles the galactic-halo-field-like chemical composition. 2P stars then formed from the polluted material processed by high-mass 1P stars and, depending on the nature of these polluters, different formation scenarios have been hypothesized.

The scenario that probably has received the most attention in the literature is the *Asymptotic Giant Branch* (AGB) scenario (Cottrell et al. 1981; Dantona et al. 1983; Ventura et al. 2001), considering the fact that many aspects related to this scenario are also included in many other scenarios. According to this scenario, 1P formed from the first burst of star formation within the proto-GC, hence 1P is the first generation of stars of a GC. Core collapse SNe explosions combined with the associated feedback from high-mass stars (greater than $8 -$

10 $M_\odot$), in the first Myrs, removed the pristine material, left from the 1P, together with the Fe-peak element produced by the core collapse SNe themself. After $\sim 30\ Myr$, the intermediate-mass stars (between $\sim 3 - 4$ and $\sim 8\ M_\odot$) evolved through the AGB phase, experience the Hot-Bottom-Burning (HBB), a phenomenon in which the convective envelope reaches regions with temperature higher than $\sim 30 - 40 \cdot 10^6\ K$, sufficient to trigger p-capture processes. Due to the convective envelope, the p-capture products are mixed in the envelope and brought into the upper layers. Moreover, during the AGB phase, the star also undergoes the so-called *Dredge-Up*, in which the convective envelope, similarly to the HBB, penetrates towards the innermost layers of the star, reaching the region previously processed by the CNO-cycle, therefore the products of the CNO-cycle are mixed in the envelope and through convective motions, they are brought up to the surface. In the final stages, the AGB stars experience a strong stellar wind, which ejects the upper layers (enriched in CNO-cycle and p-capture products) into the cluster. The ejected material does not have enough kinetic energy ($\sim 10 - 30\ km/s$, Loup et al. 1993) to overcome the potential well of the cluster, thus the polluted gas rapidly cools down and mixes with pristine material and finally starts to sink toward the center of the cluster, where it will form 2P stars. However, this scenario is not able to reproduce properly the Na-O anti-correlation, and for this reason, it requires a dilution of the AGB yields with the pristine material, which 1P stars are composed of. This pristine material needs to be accreted from the field since it is ejected outside the cluster as a consequence of the SNe explosion.

Other possible polluters are massive stars, which undergo hot hydrogen burning in their core while they evolve along the MS. Nevertheless, the products of the hot hydrogen burning form in the lower layers of the stars, hence it is unlikely that this material can reach the surface and be ejected outside the star because, in these stars, only the central regions are convective. However, according to the *Fast Rotating Massive Stars* (FRMS) scenario (Decressin et al. 2007; Decressin, Charbonnel & Meynet 2007) , if these massive stars are rapidly rotating this problem can be overcome as a result of rotation that can induce the mixing of the material inside the star and this polluted material, from which the 2P will form, can be released in the surroundings through a slow mechanical wind in the equatorial regions. Also, in this case, the polluted material has to be diluted to account for the 2P stars' chemical composition. But this problem can be solved considering the fact that this mechanism takes place when the cluster is much younger ($\lesssim 10 - 20\ Myr$) compared to the AGB scenario, therefore there is still present pristine gas left from the 1P.

Another possible way for massive stars to be able to eject the products of hot hydrogen burning is when they are in a binary system. de Mink et al. (2009) proposed that massive interacting binaries could produce the polluted material from which the 2P will form later on. They modeled the evolution of a 20 $M_\odot$ star interacting with a 15 $M_\odot$ and they found that this binary system expels virtually the entire envelope of the primary star, which would correspond to $\sim 10\ M_\odot$ of processed material, and this material has the same chemical patterns observed in 2P stars (e.g. Na-enriched, O-depleted, etc.). An interesting result about this scenario, which is called *Massive Interacting Binaries* (MIB) scenario, is the fact that the yields from a binary system depend on several parameters, e.g. the interaction time, the mass ratio, and the total mass of the system, the orbits of the components, etc. Hence, it could reproduce
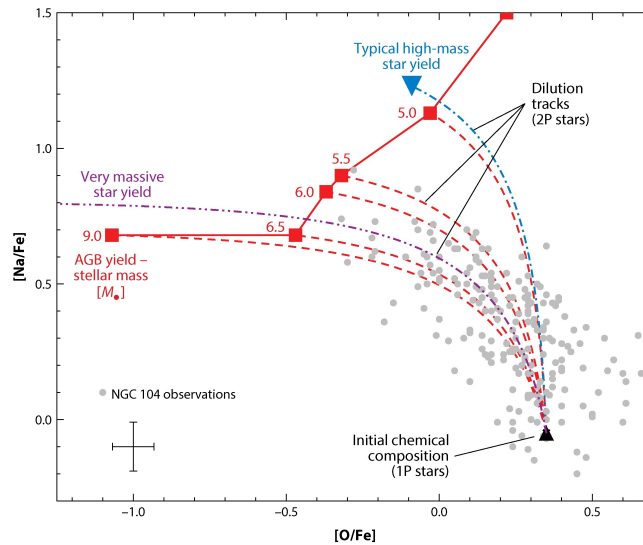
Figure 1.4: A schematic view of the dilution model. In the figure we can see the yields produced by three different polluter candidates: AGB yields (from D'Ercole et al. 2010) represented with red squared for different stellar masses, typical high-mass star ($\sim 20\ M_\odot$) yields represented with the blue upside-down triangle (from de Mink et al. 2009) and very massive star ($\sim 5 \cdot 10^4\ M_\odot$) yields in purple (off to the left of the figure, from Denissenkov & Hartwick 2014). grey points represent 2P stars of 2P stars from NGC 104 (data from Roediger et al. 2014) (image from Bastian et al. 2018).

in principle the variety of GCs.

Considering that dilution is needed to explain the chemical patterns observed in GCs, in particular for *AGB* and *FRMS* scenarios, several dilution models were developed with the aim to explain the such inconsistency. Figure1.4 shows the dilution effect on the chemical composition for three formation scenarios, the *AGB*, the *FRMS*, and the *Very Massive Stars* (VMS) (see Section 1.2.2). Focusing in particular on the *AGB* scenario, in Figure 1.4 the red squares represent the expected yield if only AGB stars are considered, for different star masses, and we can see that they produce an O-Na correlation. If dilution with pristine material is taken into account, the dilution track (dashed red line for the AGB model in Figure1.4) can explain the chemical abundance of 2P stars. Indeed, in Figure, 2P stars belonging to NGC 104 (from Roediger et al 2014) are displayed with grey dots and we can see that the dilution tracks reproduce the O-NA anti-correlation. Hence, each 2P star position, according to the dilution model, is regulated by the relative amount of polluted material (AGB yields) and the diluting material (pristine material of 1P) from which the star formed.

All three mentioned scenarios, related to the Multiple Generations scenarios, have a common problem: the so-called   *"Mass-budget problem"*, which is connected to the predominance of 2P stars. Indeed, considering the fact that only a minor fraction of the 1P initial mass forms 2P stars, in order to explain the predominance of 2P stars in GCs (on average 1P$\sim 30 - 40\%$ whereas 2P$\sim 60 - 70\%$ of the total GC stars) it is required that proto-GCs should have been much more massive compared to the present-day GCs, from 10 to 100

times more massive. There is a possible way to mitigate this problem, i.e. to reduce the required proto-GC mass but not to solve it, and this has to do with the Initial Mass Function (IMF) of the 2P. A different IMF between 1P and 2P stars has been proposed by D'Ercole et al. (2010), for which the formation of 2P stars is truncated at a mass $\sim 8~M_\odot$, i.e. only stars with a mass smaller than $\sim 8~M_\odot$ can be formed. This particular IMF has several benefits: it lowers the mass budget needed for the 2P stars and eliminates the SNe pollution of 2P stars, hence it is not necessarily a mechanism to remove the metal-rich gas produced by SNe. The assumption of this possible IMF for 2P stars arise from the fact that the environment out of which 2P stars are formed is already highly populated by 1P stars with a density $\sim 10^5~M_\odot~pc^{-3}$ (Renzini et al. 2015). This environment is quite different from a molecular cloud, which is almost free from pre-existing stars (Renzini et al. 2013), so it is possible that star formation has a different mode[1] compared to what it is observed in a molecular cloud.

To summarize, with a particular IMF, typical of high-density environments, the mass budget needed to produce 2P stars is largely reduced, but the problem is still present. To solve it, it has been suggested that proto-GCs have expanded previously and during the formation of 2P stars. As the proto-GC passes closer to its host galaxy, it loses the stars placed in the external regions, which are predominantly 1P stars, through tidal interaction. According to this scenario, we would expect a correlation between the fraction of 1P stars and the distance from the host galaxy, because at larger distance 1P stars would not be stripped away from the GC. Milone et al. 2017 and Bastian & Lardo 2015 did not find any correlation between the fraction of 1P stars and the Galactocentric distance. For this reason, the *Mass budget problem* is still unsolved.

However, *"Mass-budget problem"* could have important consequences in several astronomical fields such as Cosmology and Galactic Archaeology. As a result of their high primordial mass, along with the fact that they formed at high Redshift, GCs should have had an important contribution to the re-ionization of the Universe. Moreover, if GCs really lost most of their 1P stars they would form up to $\sim 50\%$ of the halo stars (Martelli et al. 2011), resulting in the building blocks of the Milky Way (and in general the building block of galaxies).

1.2.2   Single Generation scenarios

The second generation scenario, the *Single Generation scenario*, suggests instead that 1P and 2P are coeval populations, born from the same burst of star formation. According to this scenario, polluters belonging to 1P stars eject processed material into the intra-cluster medium with kinetic energy not sufficient to overcome the potential well of the cluster, hence it cools down and start sinking toward the central regions. This material is then accreted into low-mass 1P stars, hence forming the 2P. This material has to be accreted from a star in its Pre Main-Sequence (PMS) phase, because, once the star enters its MS phase, it probably cannot accrete a significant amount of material as a result of radiative feedback and stellar winds (Bastain et al. 2013). Moreover, direct accretion of polluted material from the surroundings into a young star is unlikely to take place unless it is present a circumstellar disk of material that is able to entertain materials as it moves through the intra-cluster medium.

---

[1]Moreover, star formation in high-density regime is poorly explored so far
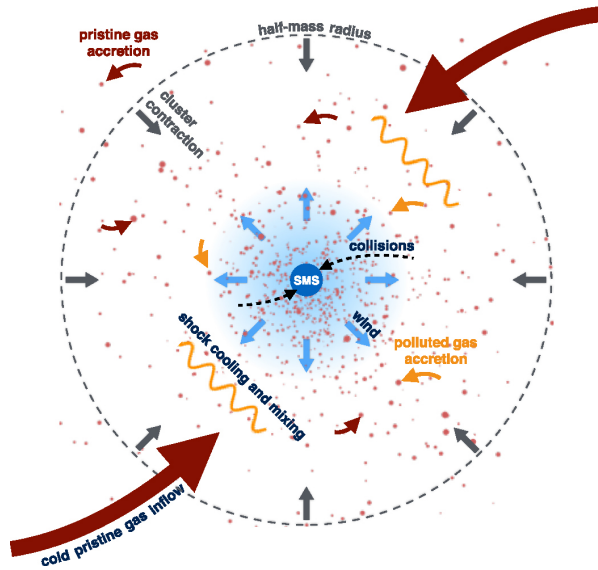
Figure 1.5: Schematic view of the SMSs formation scenario. Cold pristine gas is accreted from the GC, which undergoes an adiabatic contraction. The stellar density in the central regions reaches a value high so runaway collisions can take place, thus forming SMSs. Because of their strong stellar winds, these stars eject the polluted material which subsequently is accreted into the circumstellar disc of PMS low-mass stars to produce 2P stars (image from Gieles et al. 2018).

Considering that the PMS duration depends on the stellar mass, e.g. $T_{\mathrm{PMS}} \sim 6 \ Myr$ for a 2 $M_\odot$ star, $T_{\mathrm{PMS}} \sim 25 \ Myr$ for a 1 $M_\odot$ star and $T_{\mathrm{PMS}} \sim 90 \ Myr$ for a 0.5 $M_\odot$ star, lower mass stars can accrete polluted material for longer periods. However, as a result of the 'short' period of the PMS phase, the possible polluters have to produce and eject the processed material within the first Myr from the burst of star formation, and for this reason, the more suitable candidates as polluters are massive stars.

Gieles et al. (2018) proposed a scenario where Super Massive Stars (SMSs), stars with mass greater than ($\sim 10^3 \ M_\odot$) are the source of the polluted material. A schematic view of this scenario is shown in Figure1.5. According to this scenario, the proto-GC would go through an adiabatic contraction as a result of dynamical friction and accretion of cold pristine gas (red arrows in Figure1.5), and if the density reached in central regions is sufficiently high, SMSs can form via runaway collisions (Portegies Zwart et al. 1999). For this to happen, the density should be greater than $\sim 10^6$ stars and the accretion rate for the gas should be greater than $\sim 10^5 \ M_\odot \ Myr^{-1}$. These conditions could be reached at the formation of GCs in a high-density environment (probably achieved in the early Universe). Such massive stars are expected to be fully convective, which is required to mix the products of hot hydrogen burning that takes place in the deepest layers of the star. Because of their strong stellar winds and the radiation-driven mass-loss as a result of their high luminosity, which should be comparable to or even greater than the Eddington luminosity, SMSs eject the polluted material in the surroundings (blue arrows in Figure1.5). This material is then accreted by the circumstellar disc of PMS low-mass stars, forming thus

2P stars. An interesting result is that these SMS can eject polluted material that can be an order of magnitude greater than the maximum mass of SMSs as a consequence of the rejuvenation of these stars through continuous collisions, considering the high stellar density in central regions.

The main problem connected to this scenario is that these particular types of stars are not observed so far, neither in the near universe nor at high Redshift, even if the authors modeled a numerical simulation that shows, under certain conditions, SMS can form from runaway collisions. This formation scenario, however, could in principle explain the origin of Intermediate-Mass Black Holes (IMBHs), black holes with a mass in the range $10^2 - 10^5 \ M_\odot$, which is in between stellar mass black holes (from few up to tens of $M_\odot$) and Super Massive Black Holes (SMBHs; mass of the order $10^5 - 10^9 \ M_\odot$). The detection of IMBHs would support this scenario. Baumgardt et al. (2017) suggested the presence of an IMBH with a mass of $\sim 4 \cdot 10^4 \ M_\odot$ in the central regions of ω Centauri while Kızıltan et al. (2017) showed indirect evidence of an IMBH with a mass of $\sim 2.2 \cdot 10^3 \ M_\odot$ in 47 Tuc. However, the existence of such black holes remains uncertain and the more suitable way to detect IMBHs is through gravitational waves using the interferometers VIRGO and LIGO.

1.3   Very Low-Mass stars

So far, the vast majority of studies regarding MSPs in GCs have analyzed the spectral range mainly from the UV region ($\lambda \sim 2000$ Å) to NIR region ($\lambda \sim 8000$ Å). Here, multiple sequences can be observed only down to stellar masses $\sim 0.6 - 0.5 \ M_\odot$, whereas for populations of Very Low-Mass (VLM) stars, with mass in the range $\sim 0.5 - 0.1 \ M_\odot$, multiple sequences are quite difficult to detect because their spectral peak is located at $\lambda \gtrsim 8000$ Å and for this reason they are too faint to be accurately observed. As a consequence, the high-precision optical and UV photometry of these stars is challenging, making them among the least explored stars in the MSP context. However, as we are going to see, these stars can help us to shed light on formation scenarios of MSPs in GCs, and in particular, they can allow us to constrain the formations scenarios

Indeed, according to *Multiple Generations* scenarios (Section 1.2.1), 2P stars form in a second burst of star formation from an approximately homogeneous gas cloud composed of polluted material. On the other hand, as suggested by *Single Generation* scenarios (Section 1.2.2), 2P stars may originate from accretion processes of polluted material ejected from more-massive 1P stars. Accretion processes can be described through models, according to which, in general, the accretion rate ($\dot{M}$) depends on the accreting object mass, i.e. $\dot{M} \propto M_{\text{object}}^\alpha$ (α depends on the specif model considered). In the case of Bondi-Hoyle-Littleton accretion, the accretion rate is proportional to the square of the mass of the accreting object, $\dot{M} \propto M_{\text{object}}^2$, so that high-mass stars would have accreted more material compared to low-mass stars.

At this point we can understand the importance of VLM stars' population: if we measure the difference in chemical abundances between 1P and 2P stars in high-mass stars, e.g. in RGB or AGB, and compare it with the difference measured between 1P and 2P VLM stars, different results would favor different formation scenarios:

- The abundance difference between 1P and 2P stars in high-mass stars

and low-mass stars *is comparable* within the error bars. This result would argue in favor of *Multiple Generations* scenarios since we expect approximately the same chemical abundance between high- and low-mass stars.

- The abundance difference between 1P and 2P stars in high and low mass stars *is not comparable*, even if we take into account the error bars. This, on the contrary, would argue in favor of *Single Generation* scenarios, given the fact that the different chemical abundances between high- and low-mass stars are most likely a consequence of accretion processes.

1.3.1   Near-Infrared spectral range: a forgotten realm

The first studies of MSPs among VLM stars were published only ~ 10 years ago. Indeed, previously there were only a few space-based telescopes with suitable cameras to detect MSPs in GCs in the NIR range. One of these cameras, at that time, was the NICMOS camera onboard HST, but it was used more often to study distant objects (e.g. galaxies) instead of resolved nearby stellar populations (e.g. GCs) due to its small field of view (low resolution: 51.5×51.2 *arcsec*, medium resolution: 17.5×17.5 *arcsec* and high resolution: 11.0×11.0 *arcsec*)[2].

Another space-based telescope designed to observe in the NIR range was the *Spitzer* space telescope with the Infrared Array Camera (IRAC). This camera had a larger field of view compared to the NICOMOS camera (5.2×5.2 *arcmin*) and sensitivity over a wide range ($3 - 9.5$ μm) so in principle, it could be used to study VLM stars in GCs. However, it had larger pixels than the NICOMOS camera (1.2×1.2 *arcsec*, i.e. ~ 10 times larger) and a lower throughput and this made it not suitable for resolving crowded regions, as in the case of GCs.

This lack of a modern camera on space-based telescopes to study GCs in NIR was filled when the Wilde Field Camera 3 (WFC3) was installed onboard the HST, in May 2009. This camera, which has two channels, one for the UV/optical range (WFC3/UVIS) and the other for the IR range (WFC3/IR), has improved significantly the observational potential to detect MSPs. The detailed characteristic of this camera will be discussed in Section 2.1.

To better understand the huge improvement introduced by the WFC3 camera, Figure 1.6 it is shown the limiting point-source magnitudes reached by different HST instruments in 10 hours of exposure time, which is a proxy of the sensitivity of the instruments. From this Figure, we can easily appreciate the high sensitivity of the WFC3 camera together with its very wide wavelength coverage compared to the other HST instruments. In particular, it is worthwhile to focus our attention on the WFC3/IR channel (dark blue solid line) and compare its sensitivity to that of its predecessor, the NICOMOS camera (yellow dashed line), to understand why it was so challenging to detect VLM stars in NIR range prior to WFC3 camera.

As a result of its exceptional characteristics, all the studies concerning multiple populations among VLM stars used principally the WFC3 camera with its IR channel. Among all the available filters, the F110W and F160W filters are the most suitable to study multiple populations among VLM stars.

The F110W has a wavelength coverage between ~ 900 nm and ~ 1400 nm while the F160W filter between ~ 1400 nm and ~ 1750 nm. In the wavelength

---

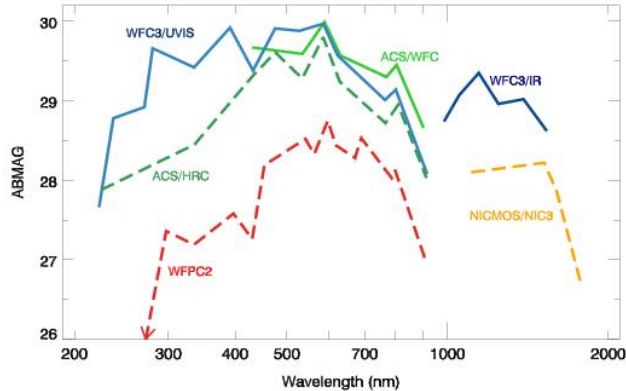[2]https://esahubble.org/about/general/instruments/nicmos/

Figure 1.6: The figure shows the limiting point-source magnitudes reached by several HST instruments in 10 hours of exposure time (image from WFC3 Instrument Handbook).

range of the F160W filter, the flux of VLM stars is affected by several molecules containing oxygen (e.g. CO, VO, OH, H_2O), with the water molecule being the strongest source of opacity. As already mentioned in Section 1.2, 1P and 2P stars show different chemical abundances and in particular 2P stars are depleted in O compared to 1P stars. As a consequence, the magnitude in the F160W filter of 1P VLM stars should be dimmer compared to 2P VLM stars. This is reflected in the m_{F160W} versus $m_{\text{F110W}} - m_{\text{F160W}}$ CMD, as the 1P stars exhibit bluer color compared to 2P stars below the MS knee. On the contrary, in stars with higher surface temperatures, i.e. above the MS knee, this effect is almost negligible (Milone et al. 2014, Dotter et al. 2015).

This effect is clearly illustrated in Figure 1.7, where, in each column, two synthetic spectra of stars with the same metallicity $[Fe/H] = -1.4$ and helium content $Y = 0.4$ but different light elements abundances (C, N, and O) are compared in the wavelength range $\sim 4500 - 17500$ Å.

The two spectra on the upper left panel represent a star with $T_{\text{eff}} = 3750\ K$, which is located below the MS knee, whereas on the upper right panel the two spectra represent a star with a hotter surface temperature, $T_{\text{eff}} = 4615\ K$, which is located above the MS knee. In both upper panels, synthetic spectra of two stars with different chemical abundances are shown, in particular, the red spectrum represents a star enhanced in N and depleted in C and O compared to the blue spectrum (the specific chemical abundances for the two spectra are displayed in the upper panels). For this reason, the blue spectrum resembles a typical 1P star chemical composition, whereas the red spectrum resembles a chemical composition of 2P star. By comparing them we can see that, as mentioned previously, the variation in C, N, and O affects largely the spectra of cold star whereas it does not alter significantly the spectra of the hot star.

In both central panels, the flux ratio between the red and the blue spectrum is represented. The difference between the two spectra are here even more evident, indeed we can see that the flux ratio for the hotter star is almost 1, which means that the two spectra are almost identical. On the other hand, the flux ratio for the colder star deviates from 1, especially for $\lambda \lesssim 8000$ Å and for $\lambda \gtrsim 14500$ Å.
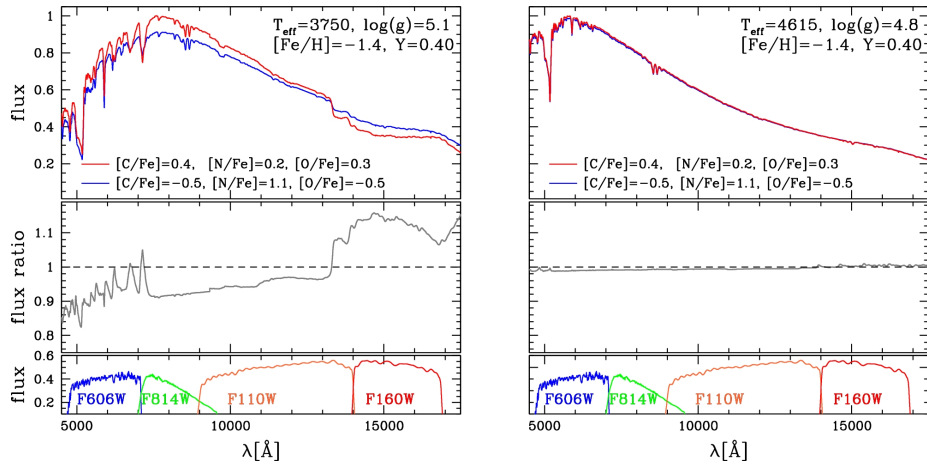
13

Figure 1.7: *Upper panels*: In both panels spectra of two stars with different chemical compositions are shown. The specific chemical composition of each spectrum is plotted in the lower part of each panel. *Middle panels*: The flux ratio between the red and the blue spectrum is displayed. *Lower panels*: Wavelength coverage of several HST filters are shown. F606W and F814W filters are used in the ACS/WFC camera whereas the F110W and F160 are in the WFC3/IR camera. Spectra displayed on the left column represent a star with $T_{\rm eff} = 3750$, $\log(g) = 5.1$ (i.e. a star located below the MS knee) whereas the spectra on the right column represent a star with $T_{\rm eff} = 4615$, $\log(g) = 4.1$ (i.e. a star located above the MS knee) (image from Milone et al. 2017).

In the lower panels, both on the right and the left column, the transmission curves of the filters F606W and F814W of the ACS/WFC camera (which will also be used in my study, see Section 2.1) and the two filters of WFC3/IR camera already mentioned, F110W and F160W, are displayed. Focusing our attention on the wavelength range of the latter filters, we can clearly see how the flux of the F160W wavelength range is higher than 1, which means that the red spectrum (i.e. 2P VLM star) is brighter than the blue spectrum (i.e. 1P VLM star) in the F160W filter and this results in a greater separation of the two populations in a $m_{\rm F160W}$ versus $m_{\rm F110W} - m_{\rm F160W}$ CMD. However, also with the F606W and F814W of ACS/WFC camera, we should be able to disentangle these different populations of VLM stars but, as already mentioned, these stars are too dim to be properly detected.

1.3.2 VLM stars in literature

As mentioned previously, very few studies concerning multiple populations among VLM stars were published. Among these studies, Milone et al. 2012 (hereafter M12) were the first to detect multiple sequences among VLM stars using F110W and F160W filters of WFC3/IR camera. Their goal was to study the multiple populations in NGC 2808, one of the most complex GC, in the lower part of the MS, i.e. below the MS knee. Prior to their study, multiple sequences in NGC 2808's MS were already observed in the optical CMD, by Piotto et al. (2007), which detected 3 different stellar populations down to the MS knee. The reddest, middle, and bluest MSs were dubbed rMS, mMS, and bMS, respectively. From isochrones fitting and taking into account spectroscopic analysis

of 122 RGB stars performed by Caretta et al. (2006), Piotto and collaborators suggested that the rMS corresponds to the first generation of stars, with halo-like abundances of He and light elements. On the contrary, the mMS and bMS correspond to a subsequent generation of stars because stars in both sequences are enhanced in He, N, and Na and are depleted in C and O. These multiple sequences can be seen in the left panel of Figure 1.3.

M12, however, found only two distinct sequences among VLM stars in NGC 2808. On the left panel in Figure 1.8, the NIR CMD of NGC 2808 is displayed and two stellar sequences can be seen, where the blue and red MSs are labeled MSI and MSII, respectively. By comparing the fraction of stars in MSI and MSII with that in rMS, mMS, and bMS and the position of stars in both the Optical and NIR CMDs, M12 suggested that the MSI is the extension of the rMS whereas the MSII is the extension of mMS and bMS, which merged together at the level of the MS knee.
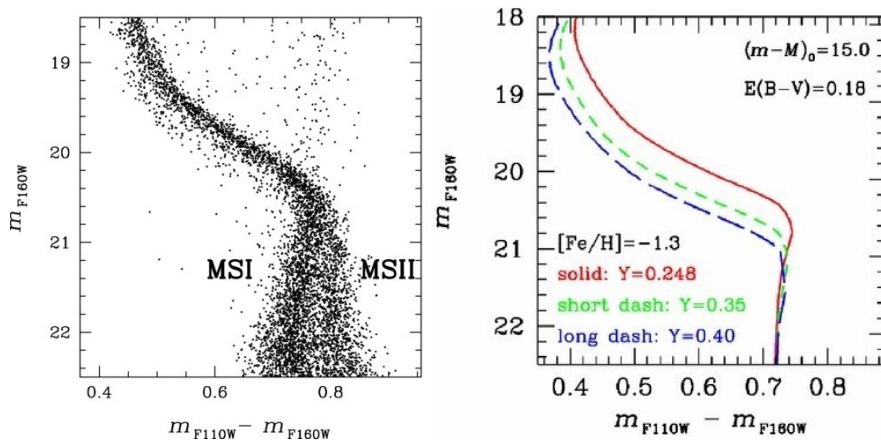

Figure 1.8: The left panel displays the CMD of NGC 2808 obtained by M12, and the two different populations labeled MSI and MSII on the red and blue sides of the MS respectively. The right panel shows three different isochrones computed by M12 to fit the three sequences detected above the MS knee. The three isochrones have the same metallicity, $[Fe/H] = -1.3$ but different He content. The red solid, green dashed and blue long dashed isochrones fit the rMS, mMS, and bMS (see text for details), respectively (image from Milone et al. 2012).

Moreover, to better characterize the properties of these two populations, M12 generated some evolutionary models to compare with the observations. First, they computed isochrones with only different He abundances (same light elements abundance) to fit the different stellar populations above the MS knee and, as expected, they found out that the three sequences found by Piotto and collaborators are consistent with stellar populations with different He abundances (left panel in Figure 1.8). In particular, the rMS is fitted with a stellar population with $Y = 0.248$, whereas mMS and bMS are fitted with isochrones with higher He abundance, $Y = 0.35$ and $Y = 0.40$ respectively. As we can see in Figure 1.8, below $m_{\rm F160W} \sim 21$, the three isochrones merge together and cannot describe the two sequences below the MS knee. M12 explain this behavior with the fact that the atmosphere models used do not account for light element variations, which affect mostly the star flux at $\lambda \gtrsim 14000$ Å, as pre-

viously seen. Indeed, accounting for the variation of C,N, and O derived from spectroscopic analysis (e.g. Caretta et al. 2006, Bragaglia et al. 2010), M12 found that the simulated color difference of the two populations below the MS knee is compatible with the observed one, proving that the two stellar populations have different chemical abundances and these are in agreement with the chemical abundance found in the populations above the MS knee.

This research is fundamental for the study of multiple populations among VLM stars in GCs because, as mentioned above, this is the first study to clearly detect MSPs in VLM stars and, moreover, it demonstrates the possibility to investigate and disentangle MSPs for these stars. Almost all subsequent studies concerning VLM stars in GCs had focused their attention on the detection and characterization of MSPs in VLM stars. However, none of them had compared the difference in light element (oxygen in particular) abundance between 1P and 2P stars measured in VLM stars and high-mass stars to test the different formation scenarios. This comparison was only done by Milone et al. 2019 (hereafter M19) studying NGC 6752. As in the case of NGC 2808, prior to their study, MSPs in NGC 6752 had been detected from the AGB down to the brighter MS (Grundahl et al. 2002 were the first to detect these MSPs). With the exception of the AGB, three distinct stellar populations were found in the RGB, SGB, and upper MS (Milone at al. 2013; Dotter et al. 2015). These three stellar populations (highlighted in a different color) are shown in the left panel in Figure 1.9 where it is shown the m_{F275W} versus $m_{F275W} - m_{F336W}$ CMD. Combining spectroscopic analysis of previous works (Yong et al. 2003, 2008 and
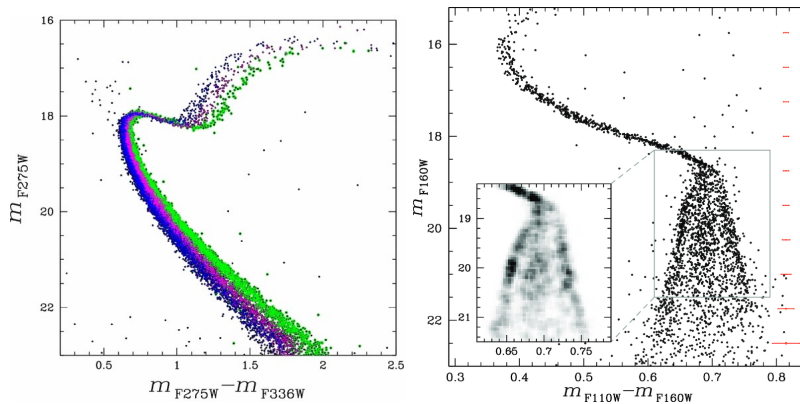

Figure 1.9: Left panel shows CMD of NGC 6752 with the different stellar populations highlighted in different colors (image from Milone et al. 2014). The right panel displays NIR CMD of NGC 6752 with the Hess diagram in the box to highlight the three different stellar populations (image from Milone et al. 2019).

Carretta et al. 2012) with the results of their multi-wavelength photometric data, Milone et al. 2014 explained the different stellar populations with the first population of stars originated from a pristine gas cloud, and a second population originated from partially polluted material. They identified the first population with the green population, which accounts for $\sim 25\%$ of the total stars, considering that its chemical composition resembles that of the Galactic halo. The magenta and blue population, which account respectively for $\sim 30\%$ and $\sim 45\%$ of total stars, represent instead a second population originating from

polluted material processed by first population stars. Indeed, stars belonging to magenta and blue populations are enhanced in He, N, Na, and Al and depleted in C and O compared to the green population. To better understand the behavior of MSPs, M19 extended the research to VLM stars in this GC using the powerful m_{F160W} versus $m_{\mathrm{F110W}} - m_{\mathrm{F160W}}$ CMD, which is displayed on the right panel in Figure 1.9.

In this CMD, the presence of MSPs can be seen only below the MS knee, where several sequences split to form a much broader MS compared to the MS above the MS knee. If we observe the CMD only (i.e. we do not pay attention to the box inside the CMD) it is a bit difficult to determine how many sequences are present. For this reason, it is usually used the so-called Hess Diagram (i.e. the box inside the CMD), which plots the relative density of stars. At a first glance at this diagram, we are able to identify at least three different stellar populations, one on the red side of the MS, another one on the blue side of the MS, and a third one in between, with the latter much broader than the first two. For this reason, this Diagram is a powerful tool to investigate and detect qualitatively MSPs in the case these sequences are not well separated. To corroborate this qualitative result, M19 compared a simulated CMD obtained with artificial stars with the observed one, and, indeed, they identified three sequences.

To better characterize the nature of these multiple sequences, M19 compared isochrones with different chemical abundances with the observed CMD (Figure 1.10). They found out that the redder MS, which is fitted with the green isochrone, is enhanced in C and O and depleted in N and He compared to the other two sequences, and in particular, the bluer MS has a higher abundance of N and He and the lower abundance of C and O among the three populations. M19 pointed out that the red MS below the MS knee is the extension of the blue MS above it (i.e. the green population in Figure 1.9) whereas the blue MS below the MS knee is the prolongation of the red MS above it (i.e. the blue population in Figure 1.9). Instead, the central MS does not change significantly the position above and below the MS knee, reaming always in between. For these reasons, below the MS knee, redder MS corresponds to 1P stars whereas the central and the bluer MS correspond to 2P stars, as expected.

For the first time, M19 compared the oxygen variation among 1P and 2P stars below the MS knee with the oxygen variation measured from spectroscopy for 1P and 2P AGB stars, which are more massive (Marino et al. 2011,2017; Nardiello et al. 2015) and they determined that the oxygen variation is almost the same in the stellar mass range $\sim 0.15 - 0.80 \ M_{\odot}$. M19 suggested that this result can be interpreted as a possible constraint to the formation scenarios of multiple populations. As a consequence, in the case that *Single Generation* scenarios are the correct ones, since 2P stars formed from accretion processes of polluted material ejected by more massive 1P stars, the accretion rate should not be proportional to the stellar mass, otherwise we should expect different oxygen abundance between high- and low-mass stars. For instance, a Bondi accretion is excluded by these results because we would expect higher oxygen abundance in high-mass stars compared to VLM stars.

Another fundamental study concerning MSPs among VLM stars is Dondoglio et al. (2022), which analyzed nine GCs and one open cluster using the filters F110W and F160W. They observed a clear bi-modality on the stellar density below the MS knee in five GCs, namely NGC 104, NGC 288, NGC 2808,
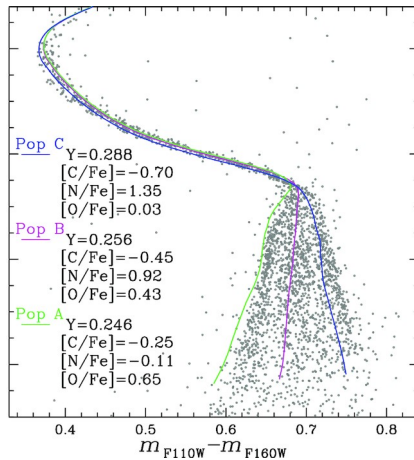
Figure 1.10: The figure shows the NIR CMD (same CMD in the right panel in Figure 1.9) with three isochrones overplotted that fit the three different stellar populations. The chemical abundances of the different isochrones are labeled in the figure (image from Milone et al. 2019).

NGC 5139, and NGC 6121 and a triple-modality distribution in NGC 6752, suggesting that these distributions are consistent with the presence of MSPs. Moreover, they compared the color spread below the MS knee ($W_{F110W,F160W}$) with the O difference ($\Delta[O/Fe]$) between 2P and 1P stars, dubbed $\Delta[O/Fe]$, inferred by Marino et al. 2019 (hereafter Ma19) by studying RGB stars, and they found the anti-correlation displayed in Figure 1.11, where $W_{F110W,F160W}$ is plotted against $\Delta[O/Fe]$. This trend suggests that the F110W−F160W color spread among VLM stars increases when the oxygen variations are larger. On the other hand, the Open Cluster NGC 6791 (black dot in Figure), in which no oxygen variations are expected (Bragaglia et al. 2014; Boberg et al. 2016), has a color spread consistent with observational errors only.

Dondoglio and collaborators measured also the Mass-Function (MF) of two chemically-different populations in NGC 2808 and M4 and found that their slopes do not vary above $\sim 0.6 - 0.8\ M_\odot$ and below $\sim 0.3 - 0.5\ M_\odot$ the MS knee. This result is in contrast with a *Single Generation* scenario where 2P stars formed through Bondi-Hoyle-Littleton accretion from 1P polluted material. Indeed, in that case, besides expecting different light-element variations between high- and low-mass stars in 1P and 2P, the different slopes of the MF are predicted, being lower for 2P stars (~ -2) and a bit higher for 1P stars (~ -1.3) (see their paper for detail).
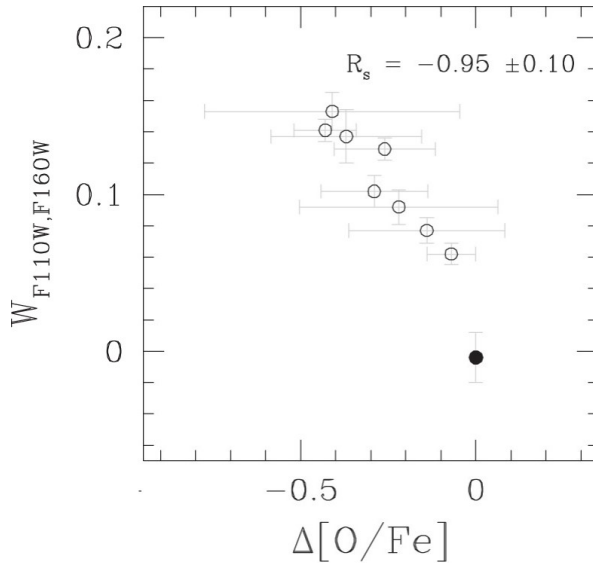
Figure 1.11: The stellar color spread below the MS knee, $W_{\mathrm{F110W,F160W}}$, is plotted against the O variation between 1P and 2P RGB stars inferred by Marino et al. 2019. In Figure is also displayed the Spearman's rank correlation coefficients for GC measurements (image from Dondoglio et al. 2022).

1.4 Thesis layout

In this Chapter, I illustrated the MSPs phenomenon in GCs and the different possible formation scenarios proposed in the literature to justify their existence, with their consequences on different astrophysical and cosmological issues. Then I described previous literature results concerning VLM stars in GCs, focusing attention on their importance to probe the MSPs phenomenon down to the almost unexplored lower part of the MS. Among the very few studies about VLM stars in GCs, I drew attention to the first study ever done about these stars, which demonstrated the possibility to investigate this region of the CMD and the information we can obtain, and the only study has done so far that had compared the difference in the oxygen abundance between 1P and 2P stars in high- and low-mass stars. This comparison can be an important test to provide some constraints on the possible formation scenarios. For this reason, in this research thesis I am going to investigate MSPs among VLM stars in NGC 288 through m_{F160W} versus $m_{\mathrm{F110W}} - m_{\mathrm{F160W}}$ CMD. Once I will detect multiple sequences, through isochrone fitting, I will be able to calculate the difference in oxygen abundance between 1P and 2P stars and compare it with the oxygen variation in 1P and 2P high-mass RGB stars, in particular with the results obtained by Jang et al. 2022. Depending on the result, I will discuss the possible consequences of the formation scenarios.

The thesis is organized as follows: Chapter 2 illustrates the characteristics of the HST instrumentation used, the photometric data set of NGC 288, and the procedure to reduce them, Chapter 3 shows the results of the data reduction and in Chapter 4 I will discuss the results with their implications for the formation scenarios and compare them with the results in the literature.

Chapter 2

Data Reduction

In this Chapter, I will illustrate the procedure carried out to obtain the photometric stellar catalog used to derive the CMD of NGC 288 and to investigate MSPs among its VLM stars. The main characteristics of this GC are summarized in Table 2.1.

Distance (pc)	$[Fe/H]$	r_c (arcmin)	r_h (arcmin)	r_t (arcmin)
8.9	-1.32	1.35	2.23	12.94

Table 2.1: Main characteristics of NGC 288: heliocentric distance, age, metallicity, core radius, half-mass and tidal radius. All values are taken from Harris 2010.

2.1 Instrumentation

Photometric data used in this research were obtained by HST, which is one of the most powerful space-based telescopes that allow high-precision photometry, fundamental to studying MSPs in GCs. HST has orbited around the Earth since 1990 at an altitude of $\sim 540\ km$, which allows for avoiding distortions induced by the atmosphere. Indeed, eliminating the presence of the atmosphere is crucial to explore very crowded regions, as in the case of GCs.

HST has a primary mirror of 2.4 m with a focal length of 57.6 m. It has a very wide wavelength coverage, from the UV ($\lambda \sim 100\ nm$) to the NIR ($\lambda \sim 1700\ nm$), and several cameras are present onboard to detect photons in the different wavelength ranges. In particular, in this research, I used data collected by two instruments: WFC3 and the Advance Camera for Surveys (ACS).

WFC3 is a fourth-generation imager installed in 2009 and it covers a very broad wavelength range ($\sim 200 - 1700\ nm$). It is composed of two different channels, one to observe in the UV and optical range (WFC3/UVIS) and the other to observe in the NIR (WFC3/IR). The ACS instead is a third-generation imager installed in 2002, with a wavelength coverage between $\sim 200 - 1100\ nm$. It is composed of three different channels: the High-Resolution Channel (HRC), the Solar Blind Channel (SBC), and the Wide Field Channel (WFC). Among these, I reduced data obtained with the following channels:

- **WFC/IR**. It has a field of view of $136 \times 123\ arcsec^2$ with a pixel scale of $0.13 \times 0.13\ arcsec^2/pixel$, which allows very high-resolution observations. The CCD, made of HgCdTe, has a total of 1024×1024 pixels (but only 1014×1014 are active). It detects photons with a wavelength between 800 and 1700 nm. Moreover, it has excellent sensitivity and also exceptional temporal and spatial photometric stability ($\gtrsim 99\%$, Kailrai et a. 2011).

  Among the available filters, as mentioned in Section 1.3.1, I used data acquired through the filters **F110W** ($\lambda_{min} \sim 883\ nm,\ \lambda_{max} \sim 1412\ nm$) and **F160W** ($\lambda_{min} \sim 1385\ nm,\ \lambda_{max} \sim 1700\ nm$).

- **ACS/WFC**. It has a greater field of view, $202 \times 202\ arcsec^2$, and higher resolution compared to WFC3/IR, with a pixel scale of $\sim 0.05 \times 0.05\ arcsec^2/pixel$. There are two aligned CCDs, made of SITe, with a size of 2048×4096 pixels each (4096×4096 pixels in total). It is sensible to photons with a wavelength between $\sim 350\ nm$ and $\sim 1100\ nm$.

  Among the available filters, I used data obtained using the filters **F606W** ($\lambda_{min} \sim 462\ nm,\ \lambda_{max} \sim 718\ nm$) and **F814W** ($\lambda_{min} \sim 687\ nm,\ \lambda_{max} \sim 963\ nm$).

2.2 Data set

The photometric data used in this research were collected by HST as part of the programs 12193, for the F606W and F814W filters, and 16289, for the F110W and F160W filters, with J.W. Lee and A. Milone as principal investigators, respectively. Information about fits files obtained with WFC3/IR are illustrated in Table 2.4 and 2.3 for the F160W and F110W filters respectively, whereas data set obtained with ACS/WFC in Table 2.2. These data sets are not sampling the center of the GC but a region $\sim 5\ arcmin$ from the cluster center, to avoid too crowded regions that are not suitable for the purpose of this research.

F606W			F814W		
Image ID	Date	Exp. time	Image ID	Date	Exp. time
jbkh01hkq	10/11/10	15	jbkh01i2q	10/11/10	150
jbkh01hnq	10/11/10	200	jbkh01i5q	10/11/10	150
jbkh01hwq	10/11/10	200	jbkh01hpq	10/11/10	10
jbkh01hzq	10/11/10	200	jbkh01htq	10/11/10	150

Table 2.2: Images obtained with ACS/WFC camera.

	F160W	
Image ID	**Date**	**Exp. time**
ieau11c2q	25/01/21	1302s
ieau12soq	17/12/20	1302s
ieau13agq	04/01/21	1302s
ieau14ppq	25/01/21	142s
ieau14pxq	26/01/21	1302s
ieau15feq	26/01/21	142s
ieau15fmq	27/01/21	1302s
ieau16zgq	30/01/21	142s
ieau16zhq	30/01/21	1302s
#ieau16znq#	30/01/21	1202s
ieau19jzq	09/05/21	142s
ieau19k0q	09/05/21	1302s
ieau19k5q	09/05/21	1202s

	F110W	
Image ID	**Date**	**Exp. time**
ieau11c1q	25/01/21	142s
ieau11c9q	25/01/21	1202s
ieau12snq	17/12/20	142s
ieau12stq	17/12/20	1202s
ieau13afq	04/01/21	142s
ieau13baq	04/01/21	1202s
ieau14q3q	26/01/21	1202s
ieau15fsq	27/01/21	1202s

Table 2.3: Images obtained through the F110W filter.

Table 2.4: Images obtained through the F160W filter. The image between the hash in the Table, ID : ieau16znq, is damaged and therefore it will not be used in this research.

2.3 Data reduction

In this Section, I will illustrate the procedure used to create the stellar photometric catalog for NGC 288. In the data reduction, I used several FORTRAN programs all developed by J. Anderson.

WFC3/NIR photometric data (_flt.fits files) are already calibrated and flatfield corrected, whereas ACS/WFC data (_flc.fits files) are also corrected for the low charge-transfer efficiency (CTE) of the detector (Anderson & Bedin 2010). In ACS/WFC files retrieved from the HST archive, the image of the two CCDs[1] are overlapped and therefore cannot be used directly. The two images can be disentangled using the FORTRAN program *flt2wj2*, which creates an image aligning the two images obtained from each CCD.

2.3.1 Effective Point Spread Function

Considering that the aim of this research is to detect VLM stars to study MSPs, we need accurate measurements of the magnitude and position of each star in NGC 288, and this can be achieved only if I have a precise PSF model for each CCD.

Indeed, a PSF model represents the distribution of the light of a source, a star in our case, in the CCD after being processed by the telescope. On the other hand, a stellar profile in the CCD is represented as a step function, which describes the stellar flux detected in each pixel (in Figure 2.1 the flux profile of a star in three adjacent pixels is shown as example). However, this step function, i.e. the stellar profile, can be fitted by different PSF models if the

---

[1]As mentioned in Section 2.1, the ACS/WFC CCD is composed of two separated rectangular CCDs.
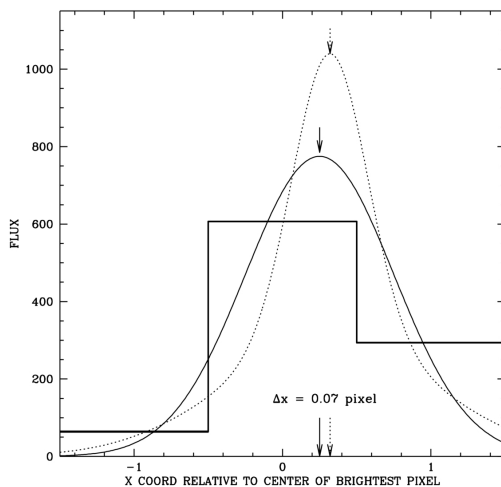
Figure 2.1: The histogram shows the flux value of a star detected in three adjacent pixels in a CCD. However, this profile can be fitted with different PSF models, which are displayed with black and dotted curves. As we can see, these PSF models have different peak positions (i.e stellar position) and different peak values (i.e. stellar flux) (image from Anderson & King 2000).

exact position of the star within the pixel is not known a priori. Different PSF models yield different measurements of the stellar position and flux, and if these models are not sufficiently accurate we would obtain an inaccurate estimation of stellar parameters. For this reason, obtaining a precise stellar PSF model for each CCD is crucial for the purpose of this research, and in general to retrieve accurate measurements of stellar position and flux.

To do that, an accurate PSF model of our CCD is needed, but we cannot obtain a precise PSF model if we do not know the exact stellar position and flux. To overcome this degeneracy I used an iterative procedure that takes advantage of some FORTRAN programs and involves the following steps. The first step is to use a library PSF model, which is not built on the actual image but is based on the CCD and filter properties instead. This model is used to obtain a first-guess PSF model for the image. The second step makes use of the latter to obtain a more accurate PSF model, which is based on the actual image. In the last step, the position and the flux of each source present in the image are measured by fitting the PSF model just obtained. Two different FORTRAN programs are used to carry out this procedure for the two cameras.

For ACS/WFC files, the first step is carried out by the FORTRAN program *img2psf*. This program calculates the first-guess PSF by fitting particular stars with an archive PSF model[2].The stars used in this first step have to be well isolated, to not be contaminated by nearby sources, and very bright but not saturated, to obtain the best-possible initial guess of the image-based PSF model. To run properly, the program requests the following parameters to select this sample of stars:

- **HMIN.** It defines the isolation index, i.e. the minimum distance (in pixels) between two sources to be considered. The value used is 20.

---

[2]One PSF model for each filter.

- **FMIN.** It defines the minimum counts' value (i.e. the flux) of a source to be considered. Since we need bright source in this first step I used 3500.

- **PMAX.** It defines the maximum count value of a source to be considered. The value used is 54000, which is right below the saturation limit.

- **QMAX.** It defines the maximum value of the Q parameter, which indicates the quality of the fit. A typical value for this parameter is 0.3.

- **NSIDES.** It defines how many regions the image has to be divided. The value used is 5.

- **PSF file**. It defines the archival PSF model to build the first-guess PSF model. I used the same PSF model for all the images of the same filter.

- **IMAGE.FITS** It defines the image on which the PSF model has to be calculated.

The program repeats iteratively the fitting procedure, using the PSF model obtained in the previous iteration, to improve the fitting itself. The program stops as soon as the PSF model obtained does not change too much between subsequent iterations. The output of this program is the PSF model, called _PSF.fits, built upon the actual image, and an example is shown in Figure 2.2. The program does not produce a single PSF model for the whole image, instead, it produces a grid of 9×10 PSFs. This is because the PSF can change shape depending on the position of the CCD as a result of optical aberrations and position-dependent charge diffusion, therefore using a grid of PSF models improve the measurement of the position and flux of each source in the image.
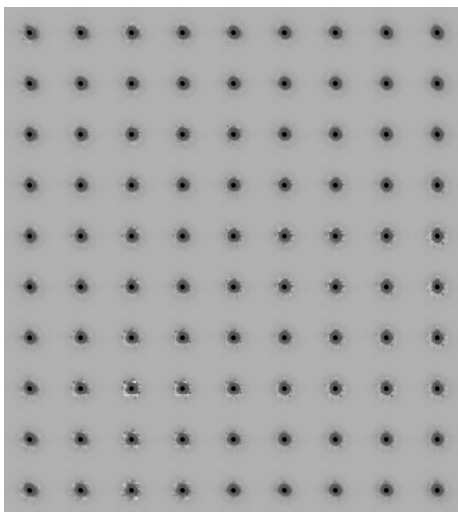

Figure 2.2: PSF model obtained with $img2psf$ for one F814W image.

In the second step, the obtained PSF model is used to measure the position and magnitude of all sources in the image. This procedure is carried out by another FORTRAN program, $img2xym$. The input parameter requested is similar to those of $img2psf$, i.e. HMIN, FMIN, PMAX, PSF file, and IMAGE.FITS

but this time I used a different value. I used a set of values that includes the majority of the sources in the image, including the very faint and the saturated ones ($HMIN = 3$, $FMIN = 50$, and $PMAX = 999999$). As a PSF file, unlike in *img2psf* where I used the same PSF model for all images of the same filters, here I used for each image the corresponding PSF model produced by *img2psf*. The output of *img2xym* is a file that contains, for all the sources detected in the image, position, magnitude, and Qfit. This latter quantity indicates the quality of the fit, and for stellar sources, it has a well-defined dependence on the magnitude, being smaller for bright stars and higher for fainter stars.

For WFC3/IR files, the procedure just explained for ACS/WFC data is performed by a single FORTRAN program, *hst1pass*. The input parameter for this program is the same: HMIN, FMIN, PMAX, PSF file, and the image to be processed. I set HMIN=3 (as in *img2xym*) whereas FMIN=0 and PMAX=999999999 in order to detect all the sources present in each image. This is because, with WFC3/IR camera, I am searching for the faintest stars within the GC so the lowest stellar flux detected (i.e. FMIN) must be 0 in order not to lose any possible star. The output of this program, similar to that obtained with *img2xym*, contains information about the position, magnitude, and Qfit value for all sources detected in the image.

So far I obtained the position and magnitude of all sources present in each image in the different filters, however, not all of these sources are stars. Before proceeding with the data reduction, I have to remove the noisy and unwanted sources. This cleaning procedure is carried out by considering the Qfit value, which is given in the file output of *img2xym* and *hst1pass* for ACS/WFC and WFC3/IR data, respectively.

Figure 2.3 illustrates the procedure identify the sources with poor photometry. I selected by eye the red curve that separates the stars that follow the dependence of the Qfit with the magnitude (that lie below it) from the sources that are clear outliers (above it). In the Figure, these latter points are mainly clustered around $m_{\mathrm{F814W}} \sim -8$. Then I created a new file where I stored all blue data points. This procedure is repeated for each image in every filter.

2.4   Photometric Catalog

At this point, it is possible to build a single photometric catalog containing all four filters considered for NGC 288. To do so, the images in each filter have to be combined together to obtain a single catalog, which will be used to create the final photometric catalog.

To merge different images of the same filter, it is necessary to put them in the same reference frame. Since the images are not perfectly aligned, therefor I used the FORTRAN program *xym2mat* to bring them into the same reference frame. This program computes the matrices for the coordinate transformations to bring each image into the same reference frame of a reference image, called master. To calculate these matrices, it searches for similar triangles, which vertices are stars, between two images, and then it rotates and translates this triangle until they coincide. This method is called *Cross Identification*.

This program requires a file that specifies the information about the images to be processed. First, I have to specify which image has to be used as a master frame and I chose, for each filter, a long exposure image in order to have the
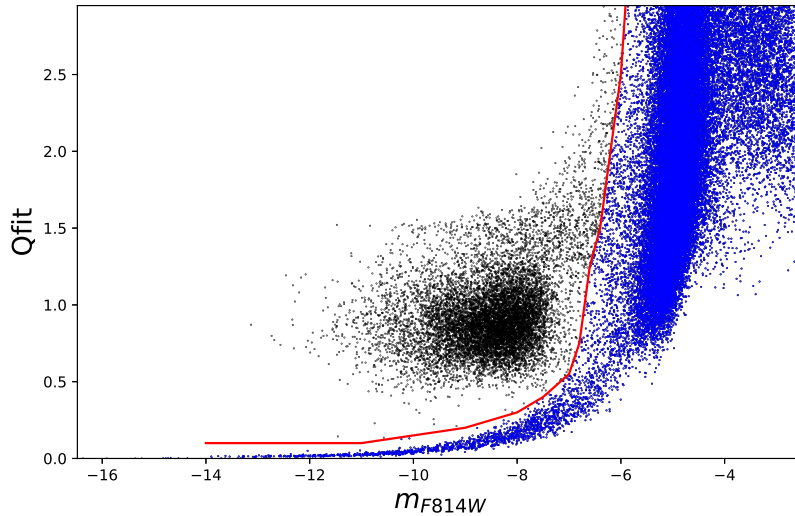
Figure 2.3: The procedure to identify poorly measured stars in one of the F814W exposures. The red line poorly-measured sources (black points) from those with high-quality photometry (blue points).

higher possible number of stars. Then I specified all the images that have to be brought in the master reference frame. An important piece of information that I need to specify is a number that indicates which camera and filter are used to obtain the images. This parameter is fundamental because each different camera and filter deform slightly and differently from the actual image. For this reason, this code indicates which CCD and filter distortions have to be applied to the exposure before proceeding with the cross-identification. Photometric data from WFC3/IR are already corrected for this effect, therefore I specified that no CCD distortion corrections are needed for WFC3/IR images. The last information needed is the position and magnitude of stars that are used to search for similar triangles between the images.

In addition to this file, the program requires an input parameter that indicates the distance, in pixels, from a star in the master image, within which the program searches for common stars in other images. In order to obtain accurate transformations, I performed two iterations of *xym2mat*. In the first one, I selected only the brightest stars, including saturated ones, to find a first-guess transformation matrix between the images and the master frame. These matrices are then used as starting point in the second iteration, where I selected only unsaturated stars since the latter are not well measured. In both iterations, I used it as an input parameter 0.45 pixel. After this second iteration, I obtain, as an output, a file that contains the correct stellar positions in the master frame for each image. A test to verify if the procedure is successful is to plot the residuals, given in the output file. These residuals are the difference in the position, in pixel, between a star in the master frame and the same star in another image, after it is brought in the master reference frame.

If these residuals are distributed circularly around 0 with a small spread, this implies that the transformations were successful. On the contrary, if the
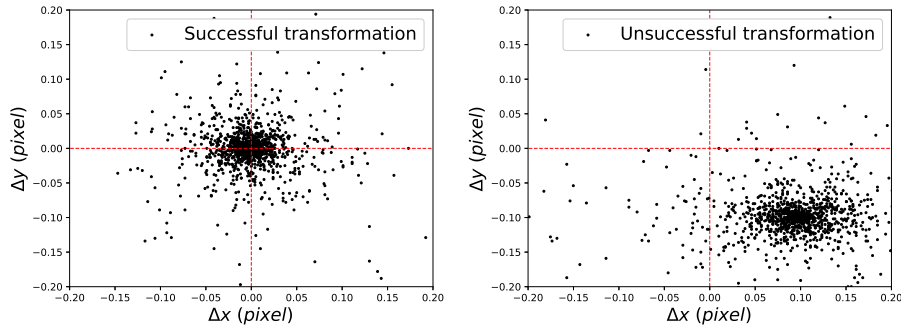
Figure 2.4: Position differences between stars in the master frame and in another image brought in the master reference frame. The left panel shows a successful transformation, characterized by a circular blob of stars centered at the origin. The right panel shows an unsuccessful transformation with points centered away from the origin showing an elongated distribution in abscissa.

residuals are not centered around 0 or they are centered around 0 but not circularly, the program did not find the correct transformation matrices and I should repeat the procedure, changing the master frame or the stars that are used to find common triangles. An example of this test is illustrated in Figure 2.4, where the residuals in x and y (in pixel) are shown. On the left panel is displayed an example of successful transformation whereas on the right panel an incorrect transformation. I carried out this test for each image in order to verify that the transformations were successful.

After obtaining these transformations, a stellar catalog can be built for each filter by averaging the position and the magnitude of all sources in all images of the same filter. This procedure is performed by the FORTRAN program *xym2bar*. This program makes use of the output files from *xym2mat* to average positions and magnitudes of common stars. This program needs a file similar to that required by *xym2mat*, which specifies which stars have to be considered. For images in both ACS/WFC filters, I selected stars with a magnitude between -13.7 and -5 for long exposure and between -99.9 and -10.65 for short exposures. For long exposure, I set the lower limit to -5 *mag* because below this threshold stars are too faint, therefore they have much larger error. For images in both WFC3/IR filters, instead, I selected those stars in the magnitude range between -15.5 and 0 for long exposure and between -99.9 and -15.3 for short exposure. This program requires an input parameter, NIMMIN, which sets the minimum number of images in which the star has to be detected in order to be considered. For ACS/WFC images is used the value 3 whereas for WFC3/IR I used 2. The output of this program is a file that contains the position, magnitude, and corresponding errors of all selected stars in the previous steps.

Now it is possible to build the photometric catalog in the different filters using the FORTRAN program *xym1mat*. This program compares a catalog in a certain filter with a reference catalog in order to find common stars and assign to them the magnitude in the two different filters.

To compare and obtain the magnitude of the two filters for each star, I

performed two iterations. In the first one, I considered only the brightest stars to create a temporary match between the two catalogs and retrieve the first guess of the transformation coefficients between the two reference frames. In the second iteration, making use of this temporary match, all stars are considered for the match-up. The output of the second iteration is a file that contains the position and magnitude in both filters of all common stars in the two catalogs. Usually, the catalog that contains the higher number of stars is used as a reference catalog, in order to not lose any stars. For this procedure, I kept the F814W catalog as the reference catalog and I matched it with the other catalogs, those of the F606W, F160W, and F110W filters, obtaining three files, one for each filter (F814W excluded since it is the reference frame).

2.5 Gaia reference frame

In the photometric catalog obtained in the previous Section, stellar positions refer to an arbitrary reference frame, the CCD frame. For the aim of this research, it is not important which reference frame but for completeness and for possible future work on NGC 288, I transformed the stellar coordinates to move from the CCD to the Gaia reference frame.

First I downloaded the catalog of NGC 288 from GAIA Data Release 3 (DR3, Gaia Collaboration et al. 2016b, 2022k)[3]. The coordinates of DR3 data are expressed in right ascension (RA) and declination(DEC), for this reason, they have to be transformed in linear coordinates (i.e. those of the CCD frame). Then, using again the program *xym1mat*, with the same procedure explained in Section 2.4 with the only exception of using the GAIA catalog as a master frame, I matched the latter with the F814W catalog, obtaining a stellar catalog with GAIA coordinates but HST instrumental magnitudes for all stars detected in the F814W filter. At this point, the same procedures used for the programs *xym2bar* and *xym2bar* illustrated in Section 2.4 are applied, using the new F814W catalog. After this procedure, I obtained a new catalog for each filter where stellar positions are in the GAIA reference frame but magnitudes are still the instrumental ones. The stellar coordinates in both the CCD and GAIA reference frames are displayed in the left and right panels of Figure 2.5, respectively.

2.6 Calibration

So far, stellar magnitudes are expressed in terms of instrumental magnitude, which have no physical meaning, thus they cannot be used for scientific purposes. For this reason, I transformed the instrumental magnitude into calibrated magnitude (m_{cal}) through the relation

$$m_{\mathrm{cal}} = m_{\mathrm{inst}} + \Delta mag + ZP_{\mathrm{filter}} + C \qquad (2.1)$$

where Δmag is the difference between the magnitude obtained through PSF photometry (i.e. the magnitude obtained in Section 2.1) and the magnitude obtained through aperture photometry (which I will discuss later on in this Section), ZP_{filt} is the zero-point in a given filter and C is the aperture correction.

---

[3]The data are available on the website `https://gea.esac.esa.int/archive/`.
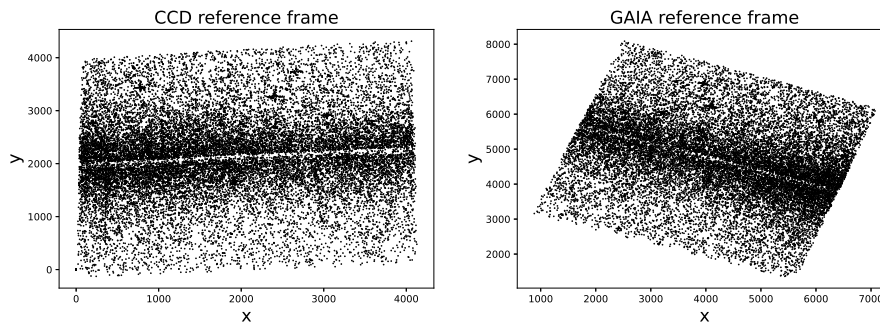
Figure 2.5: In the left panel stars are shown in the CCD reference frame, whereas on the right panel, the same stars are shown in the Gaia reference frame.

The zero-point values for ACS/WFC filters were retrieved from online utility [4] where I specified the observation date and the filters, whereas for WFC3/IR the zero-point values were retrived from another online tool[5],but whitout the need to specify the observation date. Also the values for the aperture correction were obtained from online catalogs[6]. For ACS/WFC filters I used an aperture of 0.5 *arcsec* whereas for WFC3/IR filters I adopted an aperture of 0.4 *arcsec*.

To calculate Δmag, first, a catalog with magnitude obtained through aperture photometry must be produced. For this reason, I used the FORTRAN program *drz_phot*, which performs aperture photometry, and I applied it on the drizzled images (drz.fits and drc.fits files for WFC3/IR and ACS/WFC, respectively). These are images with an exposure time of 1 *s*, thus the count value in each pixel represents actually the number of counts per unit second.

This program measures the aperture magnitudes in these images, and it requires some parameters that specify which sources have to be considered to carry out aperture photometry, which are the minimum distance between two sources to be considered (HMIN), minimum and maximum flux of the source(FMIN and PMAX) and the image to be analyzed. I set them in order to consider only bright and isolated stars. Moreover, concerning aperture photometry, I specified the aperture radius and the inner and outer radius of a ring centered around stars to measure the sky level. The choice of the aperture radius comes from a compromise between collecting as much as possible stellar flux (so by setting a very large value) and avoiding flux contamination from nearby stars (so by limiting its value). For ACS/WFC, I set $HIMN = 10$, $FMIN = 0.1$, and $PMAX = 9999$ for the sources, whereas I set 10 pixels for the aperture ring (which corresponds to an aperture of 0.5 *arcsec*), 14 pixels (0.7 *arcsec*) and 20 pixels (1 *arcsec*) for the inner and outer radius of the ring, respectively, to measure the sky. For WFC3/IR, the parameters to specify which stars to consider are the same as ACS/WFC, while I set 3 pixels as the aperture photometry radius ($\sim$ 0.4 *arcsec*) and for the sky level, I kept the same values used for ACS/WFC. The program gives as output a file where the positions and

---

[4]https://acszeropoints.stsci.edu/

[5]https://www.stsci.edu/hst/instrumentation/wfc3/data-analysis/photometric-calibration

[6]For ACS/WFC filters from https://www.stsci.edu/hst/instrumentation/acs/data-analysis/aperture-corrections and for WFC3/IR filters from https://www.stsci.edu/hst/instrumentation/wfc3/data-analysis/photometric-calibration/ir-encircled-energy
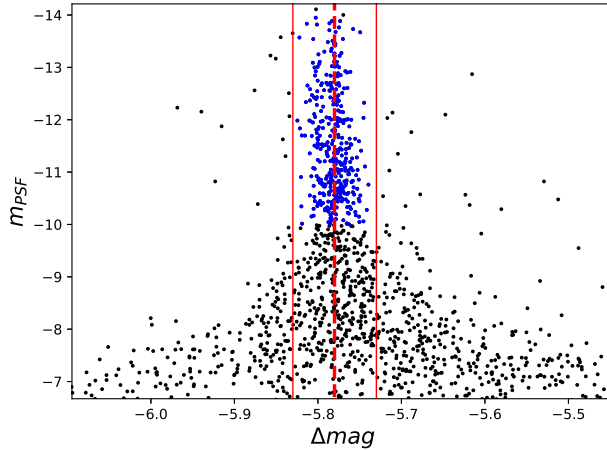
Figure 2.6: In figure it is illustrated the m_{PSF} versus Δmag used to obtain the calibration value for Δmag. Blue points represent bight and well-measured stars used to obtain an estimation of Δmag. The Red dashed line indicates the median value used for the calibration whereas the red lines represent the interval in Δmag considered for this estimate.

magnitudes of the detected stars are given.

The second step is to link these files, one for each filter, to the corresponding stellar catalog obtained with PSF photometry through *xym1mat*, with the same procedure already explained (first consider only bright stars and then all stars). At this point, I obtained the value Δmag using a user-provide python code. This code computes the difference of stellar magnitude obtained through PSF photometry and aperture photometry, considering only the difference for the brighter and better-measured stars. Then I calculated the median of these magnitude differences and I used the resulting value as Δmag in Equation 2.1. This procedure is illustrated in Figure 2.6, where m_{F606W} versus Δmag is shown for F606W photometric data. First I selected by eye the brighter and better-measured stars, which form a peak around the median value of Δmag. Then I set a range for the magnitude difference to not include stars that are too distant from the central peak and a lower limit for the magnitude to include only the brighter stars. In Figure 2.6, these stars are plotted with blue points. Then I calculated the median (represented with the red dashed line) of these stars, obtaining the value that I use as Δmag for the calibration. I repeated this procedure for all the filters. At this point, I can calibrate the magnitudes from instrumental to the Vega magnitude system.

2.7 Photometric zero point variations

Two other effects on the photometric data must be considered before proceeding with the data analysis; the differential reddening, which is associated with the presence of dust and gas on the line of sight, and the PSF variation, caused by unmodelable PSF variation.

2.7.1 Differential reddening

When interstellar dust and molecular clouds are preset between the observer and the astronomical source, the light coming from the latter can be absorbed. This absorption, called *extinction*, appears in the CMD as a shift of the source towards redder color and fainter magnitude compared to its actual position. Therefore, I have to correct the stellar magnitude obtained in the previous Chapter for this effect, otherwise, I cannot obtain accurate results.

If we are observing in a given wavelength λ, the difference between the observed magnitude (m_λ) and the intrinsic one (m_0) of the source is

$$A_\lambda = m_\lambda - m_0 \tag{2.2}$$

and it is called *interstellar absorption*. The absorption is wavelength-dependent, in particular, it is larger for shorter wavelength, i.e if $\lambda_2 < \lambda_1 \Rightarrow A_{\lambda_2} > A_{\lambda_1}$. Then, if we are observing in different bands, the difference between the interstellar absorption in the two different bands, for the same astronomical source, is expressed by the *color excess* defined as

$$E(\lambda_1 - \lambda_2) = A_{\lambda_1} - A_{\lambda_2} \tag{2.3}$$

which represents the difference between the apparent color and the intrinsic color, in particular, the extinction tends to make the color of an astronomical source redder.

If $\lambda_1 = 4361$ Å and $\lambda_2 = 3663$ Å, i.e. the B and V band in the Johnson-Cousins photometric system, the color excess $E(B-V)$ is called *reddening* and it is used to derive the interstellar absorption in different wavelength through the relation

$$A_\lambda = k_\lambda E(B - V) \tag{2.4}$$

where k_λ depends on the wavelength and its value can be retrieved from the online catalog for all the filters of HST. For the filters used in this research, the values are $k_{\text{F110W}} = 1.0155$, $k_{\text{F160W}} = 0.6293$, $k_{\text{F606W}} = 2.8782$ and $k_{\text{F814W}} = 1.8420$. To correct for extinction the only parameter needed is the reddening value. However the latter is not constant but it can change within the Field of View as a result of the inhomogeneous distribution of dust and gas clouds, even in the case we are observing a small portion of the sky. This change in the extinction value is referred to as Differential Reddening (DR) and can have a serious effect on photometry because it may introduce an additional spread in the CMD. If DR is quite strong, this spread would reduce significantly the accuracy of our photometric data, limiting the information about MSPs that we can obtain.

To estimate the effect of DR, with the aim of minimizing its possible influence on the photometric data, I adopted the iterative approach developed by Milone et al. (2012), which is illustrated in Figure 2.7(taken from their paper for simplicity), composed of three main steps which are repeated iteratively.

The first step, shown in panel (a), consists in creating a new reference frame, starting from the original CMD, where the new abscissa is parallel to a vector that represents the DR vector, i.e. the shifting direction of data points as results of DR effect (red arrow), and the ordinate is perpendicular to it. The new origin O is chosen in order to create the greater possible angle between the DR vector and the MS of the GC studied. Usually, it is located just below the MSTO. In
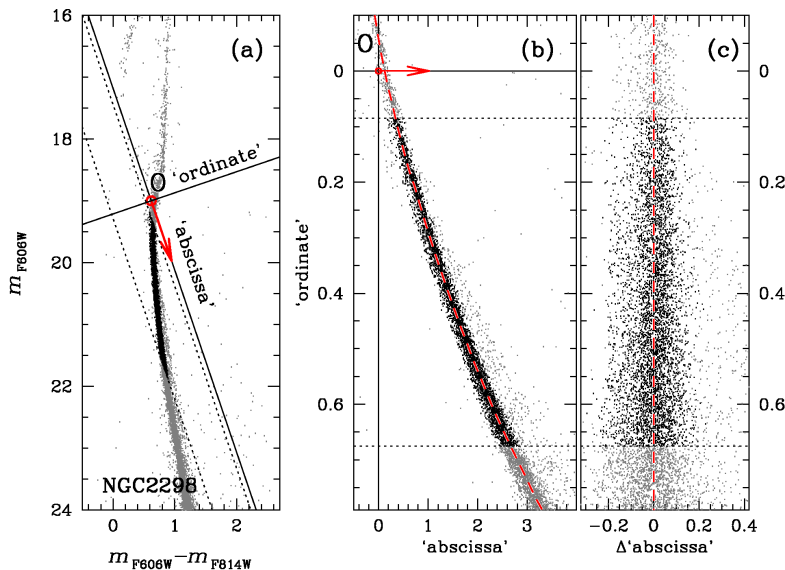
Figure 2.7: The Figure illustrates the procedure to estimate the DR correction from Milone et al. 2012 for NGC 2298. In panel (a) the choice of the origin of the new reference frame that will be used to measure the DR is shown. The red arrow represents the DR direction and the new reference frame axis labeled 'abscissa' and 'ordinate'. In panel (b), after the rotation of the CMD, the fiducial line of the MS, shown with a red dashed line, is calculated. Panel (c) shows the last step, where the fiducial line is verticalized obtaining $\Delta'abscissa'$, which is then used to correct for DR (see text for details) (image from Milone et al. 2012).

the following, I will refer to "abscissa" and "ordinate" the new reference frame axis.

In the second step, the CMD is rotated to be aligned with the new reference frame (panel (b)). In this new reference system, a sub-sample of MS stars is selected and it will be used to measure the DR. In panel (b) this sub-sample, shown with black points, is delimited by a horizontal black dotted line. This MS portion is then used to derive a fiducial line, shown with a dashed red line, which is obtained by dividing the selected MS stars into bins of 0.4 mag each, measuring their median in abscissa and ordinate and then fitting these points.

Finally, in the last step, shown in panel (c), the DR is measured. To do so, it is calculated the distance of each star from the fiducial line, defined as Δ"abscissa", and this quantity is plotted against its ordinate value. The Δ"abscissa" value represents a reasonable estimate for DR because the selected stars, as mentioned in the first step, are located in a region of the CMD where the MS forms the greater possible angle with the DR vector. As a consequence, it is easier to disentangle the shift in the magnitude and in color caused by DR with respect to the shift due to photometric error in this reference frame.

To apply the correction for DR, for each star (target) in the CMD, it is calculated the median value of Δ"abscissa" for the nearest stars, to the target star, that is present in the sub-sample defined in the second step. Usually between 30 and 100 stars are considered, depending on the dataset. In my case, I used the nearest 30 to the target star to measure the DR because my
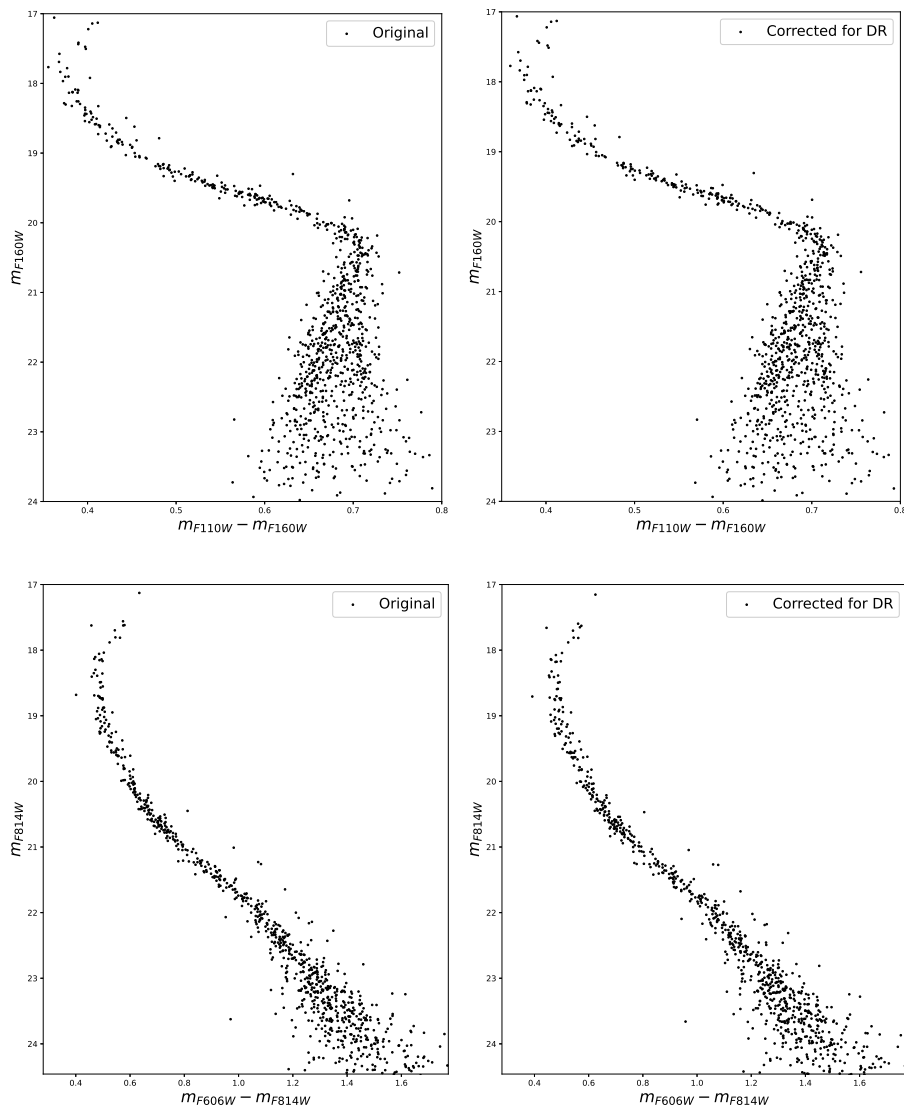
32

Figure 2.8: *Upper panels*: the original NIR CMD is shown in the left panels whereas the CMD corrected for DR in the right one. *Bottom panels*: the same as in upper panels but with the optical CMD. The correction for DR is almost negligible, as we can see by comparing the corrected and the original CMDs.

sample is not too numerous. Then, after obtaining the corrected CMD, the procedure is repeated but this time starting with the corrected CMD to improve the estimation of the DR. The iterations are stopped when the new CMD does not change significantly from the CMD obtained in the previous iteration.

Since the amount of absorption due depends on the wavelength, the effects of reddening are minimum in F160W and maximum in F606W. For this reason, the $m_{\rm F606W} - m_{\rm F160W}$ color would maximize the information on differential reddening. Nevertheless, I found out that errors associated with the reddening determination are larger than the amount of DR itself, therefore the quality of the Optical and NIR CMDs for NGC 288 does not benefit from DR correction. This can be seen in Figure 2.8 where the original (on the left panels) and corrected (on the right panels) Optical and NIR CMD are illustrated. For this reason, I did not correct the CMDs for it.

2.7.2 PSF variations

When the DR correction is smaller than $0.10\,mag$, as in my case, a correction for unmodelable PSF variations in the CCD is applied instead, which is caused mainly to focus changes. These variations introduce a small shift in the CMD location of stars, as in the case of DR, depending on the position of the CCD. However, this effect does not have a preferential direction as the DR, but shifts stars randomly. I expect his effect to be more evident in the color direction since the magnitude range in my CMD ($\sim 8\ mag$ for both CMD) is way bigger than the covered color range (~ 1 for the optical CMD whereas ~ 0.4 for NIR CMD). In the color direction, the expected variation due to this affects ~ 0.005 mag (Anderson et al. 2009; Milone et al. 2010). For this reason, the only difference with respect to the procedure explained in Section 2.7.1, is that I did not rotate the CMD along the DR direction but I kept it with the abscissa corresponding to the color direction since I want to apply the PSF correction essentially for color variation. Considering that the WFC3/IR camera has a poorer quality compared to ACS/WFC, I would expect that the correction for PSF variation should be larger for WFC3/IR filters. However, even using the $m_{\rm F160W}$ versus ($m_{\rm F110W} - m_{\rm F160W}$), the correction is negligible (lower than $0.001\ mag$) suggesting that the major contribution of the PSF variation was already corrected by the $ZP_{\rm filter}$ parameter in Equation 2.1.

This procedure provides high-quality photometry and astrometry. This dataset will be used in the next Chapter to detect and characterize MSPs in NGC 288.

Chapter 3

Results

In this Chapter, I will analyze the photometric catalogs to identify and characterize MSPs in NGC 288. In particular, I investigate for the first time the multiple populations among the VLM stars, below the MS knee.

The Chapter is organized as follows. In Section 3.1, I qualitatively analyze the m_{F814W} versus $m_{F606W} - m_{F814W}$ CMD and the m_{F160W} versus $m_{F110W} - m_{F160W}$ CMD to detect the main features associated with multiple populations. In Section 3.2, I will disentangle the different stellar populations of NGC 288, whereas in Section 3.2 I will compare the CMDs with isochrones to better characterize the different stellar populations. In Section 3.4, I will finally measure the O variation between the MSPs, making use of synthetic spectra.

3.1 CMD of NGC 288

The Optical CMD is shown in the left panel in Figure 3.1, where I plot m_{F814W} versus $m_{F606W} - m_{F814W}$ for NGC 288 stars. This diagram extends from the SGB to the lower part of the MS. Due to the observational errors, it is not possible to approach the VLM regime. From this CMD, however, as I would expect, I can identify MSPs, neither in the upper MS nor in the lower MS.

Indeed, the fundamental CMD for the purpose of this research is the m_{F160W} vs $(m_{F110W} - m_{F160W})$ CMD, shown in the right panel in Figure 3.1. The first difference with respect to the optical CMD is the presence of the MS knee. According to theoretical models (e.g. Baraffe et al. 1997, Calamida et al. 2009, Bono et al. 2010) and from observations (Milone et al. 2012, 2013, 2017; Dondoglio et al. 2022), this is a common feature for VLM stars, in particular with mass smaller than $\sim 0.5 - 0.4 \ M_{\odot}$, in the NIR CMD.

Just below the MS knee, the stellar colors tend to be constant, i.e. stellar tracks are vertical in the CMD (especially for 2P stars, as we are going to see in the following), and this is caused by two competing effects. The first is related to the decrease of the effective temperature combined with the increment of the radiative opacity whereas the second one is connected to the increase of the collisional-induced absorption (CIA) of molecular hydrogen in the IR band. The first one tends to shift the star towards redder color, and the second one instead, through the CIA of H_2, tends to make the stellar color bluer.

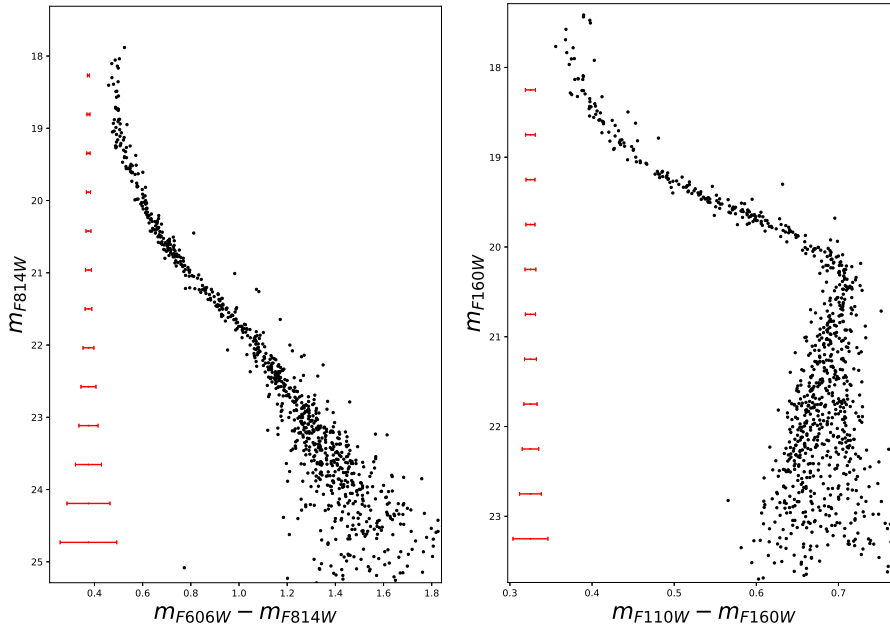The color spread below the MS knee, unlike in the case of the optical CMD,

Figure 3.1: The optical and NIR CMD of NGC 288 are displayed in the left and right panels, respectively. Error bars are shown in red.

cannot be justified by photometric errors only, which are displayed in red on both panels in Figure 3.1. If this color spread is not caused by photometric errors, it is likely connected with the presence of MSPs, as also suggested by the comparison with the other NIR CMDs from the literature. In particular, this CMD exhibit a very similar structure to those shown in Section 1.3.2 (left panel in Figure 1.8 and right panel in Figure 1.9) and for this reason I would expect the presence of, at least, two different stellar populations. This idea is also corroborated by considering the properties of MSPs in GCs, in particular for the chemical composition of 1P and 2P stars. Indeed, as already mentioned in Section 1.3.1, 2P stars are depleted in O with respect to 1P stars, and since the F160W filter is sensitive to O variations, I would expect that 2P and 1P stars form a blue and a red sequence below the MS knee, respectively.

To better highlight this bimodal distribution, I plotted two histograms that illustrate the stellar density as a function of the color in two magnitude intervals. Considering that the MS below the MS knee is not vertical, I have to verticalize it with respect to a line, which separates qualitatively the two stellar populations. This line is shown as a red solid line (hereafter, red line) in the left panel in Figure 3.2. At this point, I chose two magnitude intervals, $21 \leq m_{\mathrm{F160W}} \leq 22$ and $22 \leq m_{\mathrm{F160W}} \leq 23.5$, which are delimited with the black dashed lines in the same panel. Then I verticalized the MS by defining the quantity $\Delta\,color$, which is equal to the difference between the color of the stars and the red line at the same magnitude level. A value of $\Delta\,color < 0$ represents a star that is located on the left side of the red line, whereas stars on the right side are those with $\Delta\,color > 0$. In both histograms, I also plotted also a black dashed vertical line
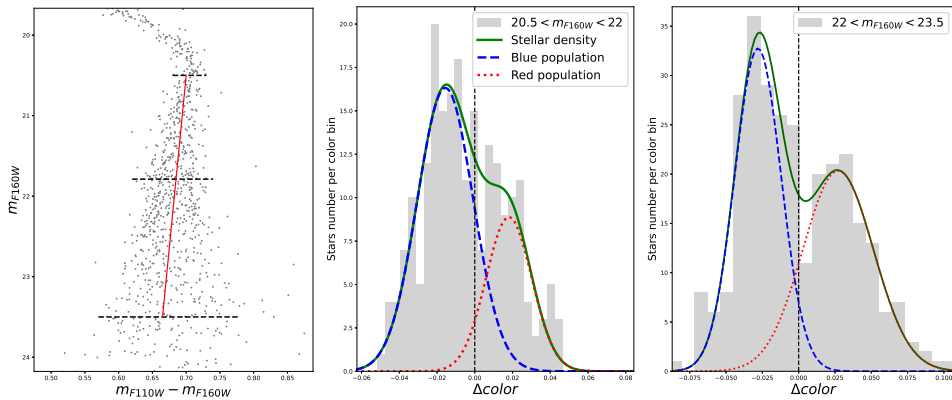
36

Figure 3.2: In the left panel I divided the MS below the MS knee, in the NIR CMD, into two intervals, the first between $20.5 \leq m_{\text{F160W}} \leq 22$ and the second $22 \leq m_{\text{F160W}} \leq 23.5$. The red line separated qualitatively the stellar population into two sub-samples of stars, a blue population on the left side and a red population on the right side. In the middle and right panels, the stellar distribution as a function of $\Delta\,color$ is shown for the two magnitude intervals defined in the left panel. Red and blue Gaussians describe the red and blue population, whereas the green solid line represents the overall trend of the stellar distribution. The black vertical line separates these two populations.

which represents $\Delta color = 0$ to separate visually the two populations. At this point I plotted the stellar density using their $\Delta\,color$ value in the two different magnitude intervals, which are displayed in the central and left panel for the interval $20.5 \leq m_{\text{F160W}} \leq 22$ and $22 \leq m_{\text{F160W}} \leq 23.5$, respectively. The total stellar density profile is shown with the green solid line whereas the black vertical dashed line separates the blue and red populations.

The presence of two stellar populations should result in a bi-modality stellar distribution. However, in the magnitude interval just below the MS knee (central panel), this bi-modality is not very clear. I fitted the blue population with a Gaussian, the blue one, and we can see that it represents the majority of the stellar population and it reproduces the main peak of the stellar distribution. I fitted also the red population with a Gaussian, the red one, however, in this case, it does not produce a distinct and clear peak in the stellar distribution, meaning that the two stellar populations are not well separated. Indeed, since these populations are located in a small color interval in the CMD, ~ 0.1, it is likely that the two populations are superimposed.

On the other hand, moving towards a fainter magnitude, the two populations are well separated. Indeed, in the right panel, we can clearly see a bi-modal distribution of the stellar density (green line), where the two peaks are well separated and correspond to the blue and red population distribution, which is fitted with the blue and red Gaussian. A possible reason for this well define separation is that, in the lower part of the CMD, the two populations are spread over a wider color interval, ~ 0.15., compared to the previous magnitude interval.
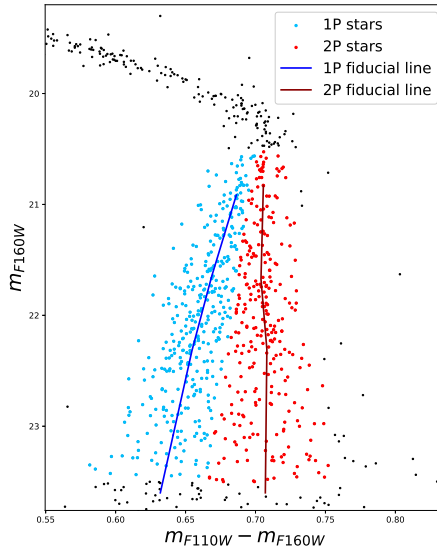
Figure 3.3: Zoom-in of the NIR CMD of NGC 288, on the lower part of the MS, from the MS knee to the bottom of the MS. Here I selected by eye 1P stars, marked in light blue, and 2P stars, marked in red, between $m_{\mathrm{F160W}} = 20.5$ and $m_{\mathrm{F160W}} = 23.5$. The Blue and the dark-red line represent the fiducial line of 1P and 2P stars, respectively, calculated as a linear interpolation of the color median values for 1P and 2P stars in four magnitude intervals.

3.2 Multiple populations among VLM stars in NGC 288

After these considerations, I identify the blue population as 1P stars whereas the red population as 2P stars, shown in light-blue and red, respectively, in Figure 3.3.

The next step consists in calculating the fiducial lines for both populations. I divided the magnitude interval between $m_{\mathrm{F160W}} = 20.5$ and $m_{\mathrm{F160W}} = 23.5$ into 4 bins and I calculated, for each population, the median of stellar color in each bin and the middle point of each magnitude interval. After identifying these points, I did a linear interpolation to draw the fiducial lines of 1P and 2P stars, which are displayed as a blue and red solid line, respectively. As we can see, the color of the red population is almost constant around ~ 0.70, whereas the blue population tends to become bluer moving toward fainter magnitudes, spanning a color range from ~ 0.63 to ~ 0.68. I truncated the selection of 1P and 2P stars at $m_{\mathrm{F160W}} = 23.5$ in order to not worsen my photometric data because below this value there are only a few stars well measured.

The total number of stars in this region is 656, with 409 of them being 1P stars, which account for $\sim 62\%$, and 247 of them being 2P stars, which accounts for $\sim 38\%$ of my sample.

In Figure 3.4 I show the selected 1P and 2P stars in all the others filter combinations in my dataset. The upper panels show the combination of F814W with the two WFC3/IR filters, F110W in left panel and F160W in right one. Bottom panels instead show the combination of F606W filter with F110W in

left panel and F160W in right panel. In each CMD 1P and 2P stars with their fiducial line are highlighted in blue and red, respectively.

The first feature that we can see is the different color spread in the lower part of the MS between CMDs built with the filter F814W (upper panels) and those built with the filter F606W (bottom panels). Indeed in the latter CMDs, the color spread is smaller compared to the first ones, but this is probably caused by the smaller error bars associated with the CMDs based on the F606W band.

Concerning the two stellar populations, in the CMDs built with the combination of the filter F606W with those of WFC3/IR (bottom panels) 1P and 2P stars are not distinguishable, which is also shown by the fiducial line that is almost superimposed. On the contrary, in the CMDs built with the filter F814W (upper panels) the two stellar populations seem to be more separate, especially in the m_{F814W} versus $m_{\mathrm{F814W}} - m_{\mathrm{F160W}}$ CMD (upper right panel). In this CMD we can see that 1P stars tend to stay on the bluer part of the MS whereas 2P stars are on the redder one.

3.3   Isochrones fitting

After the visual inspection of the two populations, to obtain the more precise information and also to calculate the difference in oxygen abundance I fitted both the optical and the NIR CMD with isochrones retrieved from Dartmouth Stellar Evolution Program (DSEP; Dotter et al. 2008) [1]. The parameters needed to DSEP to generate the isochrones are the age, metallicity ([Fe/H]), helium abundance (Y), α-elements abundance ([α/Fe]) and the instrument used to obtain the photometric data to be fitted. The metallicities considered for NGC 288 are -1.32 ± 0.02 from Carretta et al. 2009, -1.37 ± 0.04 from Koval & Gozha 2019 and -1.26 ± 0.04 from Horta et al. 2020. For α-elements abundance, I found 0.42 from Carretta et al. 2010.

Considering these values, I retrieved isochrones with ages between 12 Gyr and 13.5 Gyr with a step of 0.05 Gyr. For each isochrone, I chose a metallicity, based on literature estimates, between -1.20 and -1.40 with 0.01 step, a helium abundance that depends on the metallicity according to $Y = 0.245 + 1.5 \cdot Z$, with Z being the mass fraction of the metals, and a fixed [α/Fe] value of 0.4. These isochrones were computed for WFC3/IR and ACS/WFC filters but their magnitudes are expressed as absolute magnitude[2] M_{iso}. For this reason, to properly compare the isochrones with the observed CMDs, I calculate the corrected isochrone magnitudes, m_{corr}, through

$$m_{\mathrm{corr}} = M_{\mathrm{iso}} + (m - M) + A_\lambda \tag{3.1}$$

where $(m - M)$ is the distance modulus, defined as $(m - M) = 5 \cdot \log_{10}(d) - 5$ with d the distance of NGC 288 which is ~ 8.9 kpc (Harris 2010), and A_λ is the interstellar absorption, already seen in Equation (2.2) at the beginning of Section 2.7.

After correcting the isochrone magnitudes, I found the best-fit parameters which fit the MS in both optical and NIR CMDs. First, I started with the optical CMD to find its best-fit isochrone, obtaining the parameters reported

---

[1]http://stellar.dartmouth.edu/models/index.html
[2]The intrinsic magnitude of an object 10 pc distant from the observer
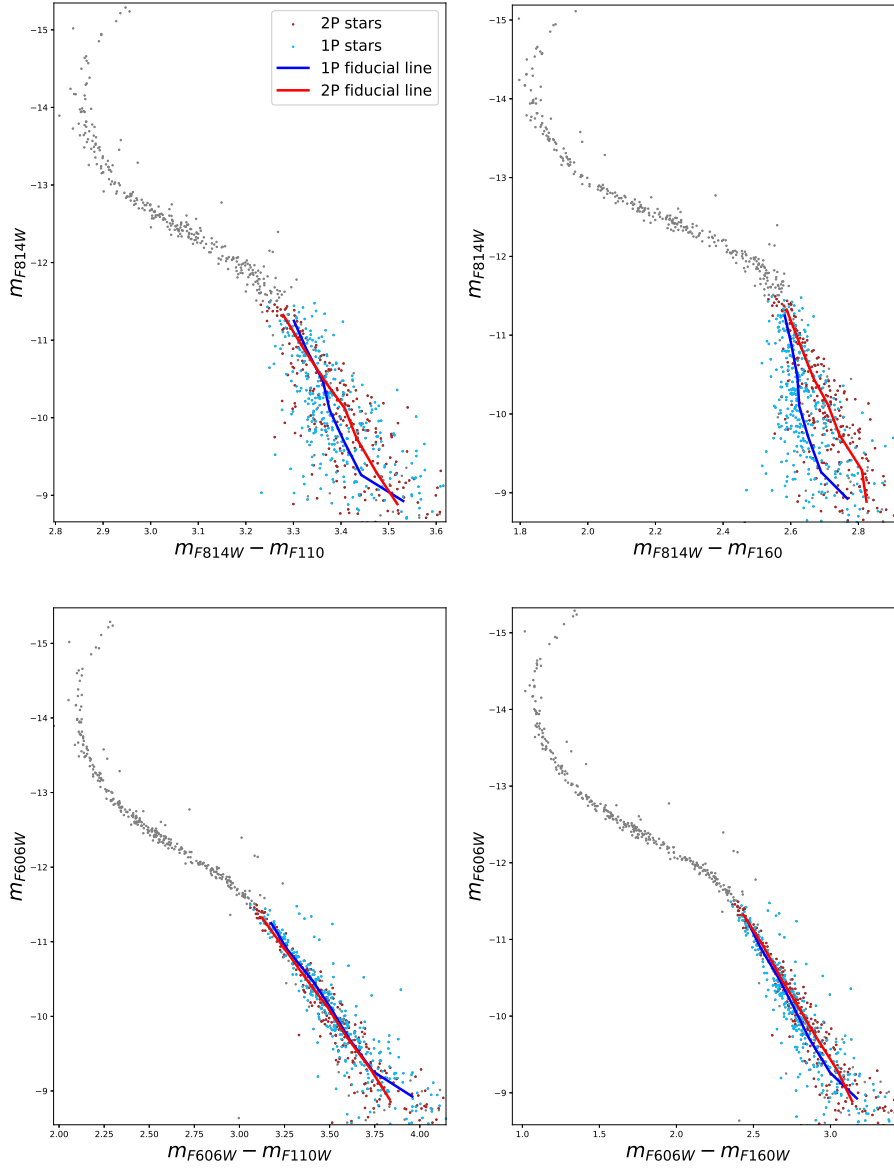
Figure 3.4: *Upper panels*: CMD built combining F814W filter with F110W (left panel) and F160W (right panels). *Bottom panels*: CMD built combining the F606W filter with the F110W filter (left panel) and the F110W filter (right panel). In each CMD, error bars are shown on the left side with the red line.

in the first row of Table 3.1 as the best to reproduce the MS trend. These values, afterward, are used as starting point to find the best-fit isochrone in the NIR CMD. I slightly changed in particular the age and the metallicity to better fit the MS just below the MSTO, and the value for the best-fit isochrone are displayed in the same Table.

Concerning the isochrone in the NIR CMD, below the MS knee, these isochrones can only qualitatively reproduce the trend of 1P stars, while 2P stars cannot be reproduced by operating on the DSEP isochrones' parameter. Clearly, this is due to the fact that they do not take into account O variations among stars, which produces the redder VLM stars sequence. The CMDs with the isochrone superimposed to the MS are displayed in Figure 3.5, with the blue line.

CMD	distance (kpc)	age (Gyr)	[Fe/H]	Y	$[\alpha/\text{Fe}]$	E(B-V)
Optical	8.99	13.40	-1.19	0.2484	0.40	0.01
NIR	8.99	13.15	-1.26	0.2479	0.40	0.01

Table 3.1: Best-fit isochrones parameter for the optical and NIR CMDs.
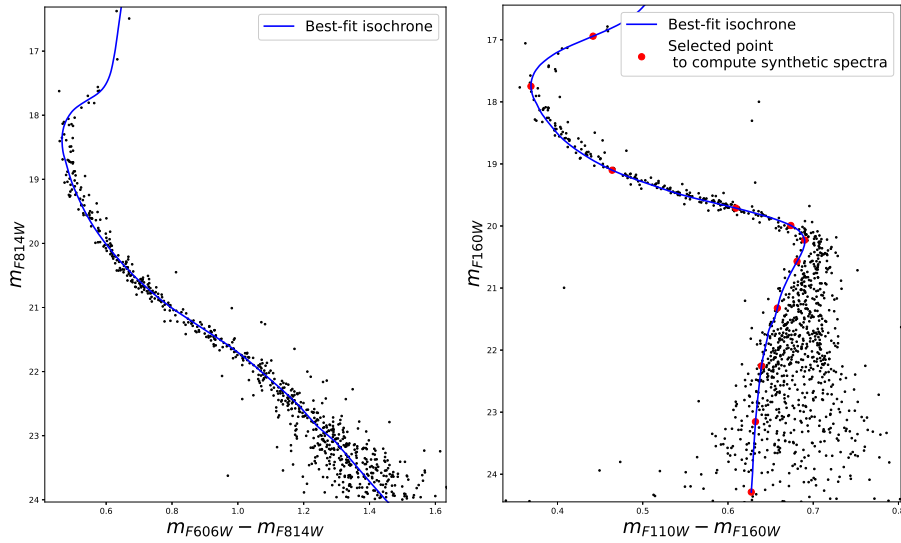

Figure 3.5: Left panel shows the optical CMD with the best-isochrone superimposed, which parameters are displayed in Table 3.1, whereas on the right panel the NIR CMD is shown with the best-fit isochrone. The blue dots are used to reproduce synthetic spectra, which procedure is explained in Section 3.4.

3.4   Oxygen variation

To estimate the amount of oxygen variation, I followed the recipe by M19. In a nutshell, I first selected eleven points from the isochrone that provides the best fit with the NIR CMD and extracted their atmospheric parameters. The values of stellar gravity and effective temperatures are used to compute synthetic spectra of 1P and 2P stars. The difference between their fluxes allowed me to evaluate how magnitudes, and therefore colors, change as a result of light-element variations. The comparison between the observed colors of 1P and 2P stars and the colors predicted by synthetic spectra with different chemical compositions is crucial to constrain the oxygen content of the distinct stellar populations of NGC 288.

Considering that, above the MS knee, I do not expect important variation in magnitude and color[3] due to light-elements variation, I selected only 5 points between $m_{\mathrm{F160W}} \sim 17$ and $m_{\mathrm{F160W}} \sim 20$ to perform these synthetic spectra because, with a greater number of points, the computational time would be much greater without obtaining useful information. On the other hand, below the MS knee, $m_{\mathrm{F160W}} \gtrsim 20$, where I expect a significant color spread introduced by oxygen variations, I selected 6 points, thanks to which I will measure the oxygen difference between 1P and 2P stars. These points are shown in red in the same NIR CMD where the best-fit isochrone is displayed (right panel in Figure 3.5).

To calculate these synthetic spectra, I assumed [Fe/H]=-1.26,[α/Fe]=0.4 (i.e. the isochrone parameter), and for each star the effective temperature and the gravity extracted in the isochrone. I provided this information to Dr. A.F. Marino who generated the synthetic spectra with SYNTHE (Kurucz & Avrett 1981) in the spectral range between $\lambda = 850$ nm and $\lambda = 1900$ nm, using atmosphere models created by Robert Kurucz (Kurucz 1993,2005; Castelli 2005).

The chemical composition of 1P and 2P stars in the RGB, in particular the O abundance, was used to reproduce the chemical composition of the selected stars. Several molecular lines were added to better reproduce the flux decrement, e.g. CO, C_2, H_2O, OH.

From the comparison of the synthetic spectra, I retrieved the magnitude variation in the F110W and F160W filters, $\Delta m_{\mathrm{F110W}}$ and $\Delta m_{\mathrm{F160W}}$ respectively, and the color difference, $\Delta color$, for a variation of $[O/Fe] = 0.2$ dex [4] for the selected stars. These quantities, together with the parameters used to generate the synthetic spectra, are displayed in Table 3.2. Moreover, the stellar mass in solar masses, $M/M_{\odot}$, and the identification number of the star in the isochrone file, EEP, are also displayed. The first star corresponds to the red point at $m_{\mathrm{F160W}} \sim 17$, i.e. the first selected isochrone point from the top, in the CMD in the right panel in Figure 3.5, and the others follow.

Stars with the EEP value between 164 and 53 represent stars located above the MS knee, with stellar mass greater than 0.5 $M_{\odot}$. As we can see, the magnitude difference in both filters due to O variation is 0 for almost all these stars, whereas this difference becomes important from the MS knee, represented by the star with EEP=49, toward fainter magnitude. This effect is more evident when considering $\Delta color$, which becomes larger towards fainter stars, whereas is

---

[3]From what we have already seen in Section 1.3.2
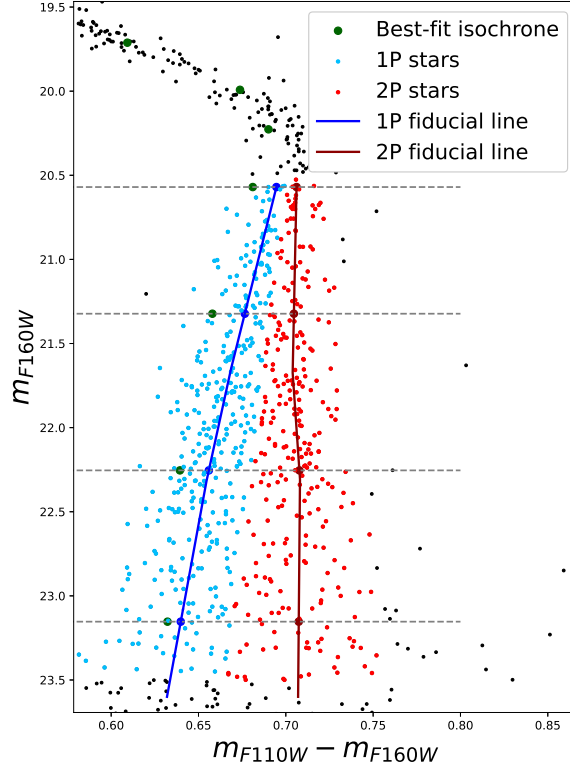[4]The value of 0.2 dex corresponds to $10^{0.2}$.

Figure 3.6: Zoom-in of the region below the MS knee where 1P and 2P stars were selected. In green are shown the isochrone points chosen to compute the synthetic spectra. The blue and red lines represent the fiducial lines of 1P and 2P stars, respectively. The blue and red dots on the fiducial line are chosen such as to have the same magnitude, displayed with horizontal grey dashed line, of the BFI points. These points will be used to measure the O difference between the two populations.

essentially 0 for stars above the MS knee. In particular, $\Delta color$ is the parameter that I used to calculate the O difference between 1P and 2P stars.

To do so, I first selected, from the isochrone, those stars that are located in the magnitude range used to choose the two stellar populations, which are the four green points shown in Figure 3.6. Then I selected those points on the two fiducial lines that lie at the same magnitude level as the isochrone points, which are displayed as the horizontal dashed lines. These points are marked in red and blue along the 1P and 2P fiducial lines, respectively. I calculated the color difference between these points and the isochrone points, $\Delta color_{\mathrm{blue}}$ and $\Delta color_{\mathrm{red}}$, thanks to which I can estimate the O difference between the 1P and 2P stars through

$$\Delta[O/Fe]_{1P-2P} = \frac{\Delta color_{\mathrm{blue}} - \Delta color_{\mathrm{red}}}{\Delta color} \cdot 0.2 \; dex \qquad (3.2)$$

where the 0.2 factor account for the fact that the magnitude and color variations calculated from synthetic spectra are due to a variation of $[O/Fe] =$

EEP	$\log(T_{\rm eff})$	$\log(G)$	$M/M_\odot$	$m_{\rm F160W}$	$\Delta m_{\rm F110W}$	$\Delta m_{\rm F160W}$	$\Delta color$
164	3.757	3.831	0.81	16.94	0.001	0.001	0.000
131	3.792	4.194	0.78	17.75	0.000	0.000	0.000
82	3.741	4.586	0.67	19.10	0.001	0.000	0.001
61	3.685	4.678	0.58	19.71	0.000	0.000	0.000
53	3.657	4.703	0.54	19.99	0.000	0.000	0.000
49	3.638	4.722	0.52	20.23	0.007	0.006	0.001
45	3.617	4.761	0.48	20.57	0.017	0.012	0.005
38	3.588	4.878	0.39	21.32	0.054	0.040	0.014
23	3.566	5.006	0.26	22.25	0.096	0.065	0.031
17	3.547	5.124	0.18	23.15	0.051	0.008	0.043
13	3.525	5.313	0.11	24.29	0.038	-0.013	0.051

Table 3.2: Magnitude variations, $\Delta m_{\rm F110W}$ and $\Delta m_{\rm F160W}$, obtained from the comparison between two synthetic spectra which have a variation of $[O/Fe] = 0.2\ dex$. The parameters used to calculate these synthetic spectra are the effective temperature, $\log(T_{\rm eff})$, and the surface gravity, $\log(G)$. EEP indicates the identification number of the stars in the isochrone file whereas $M/M_\odot$ represents the stellar mass expressed in solar mass.

EEP	$M/M_\odot$	$m_{\rm F160W}$	$\Delta[O/Fe]_{\rm 1P-2P}$
45	0.48	20.57	0.39 ± 0.01
38	0.39	21.32	0.42 ± 0.01
23	0.26	22.25	0.33 ± 0.03
17	0.18	23.15	0.32 ± 0.03

Table 3.3: The O difference between 1P and 2P stars from the comparison between the color difference of the synthetic spectra and the observed CMD. The Table also provides the stellar mass (expressed in solar masses), and an identification number.

$0.2\ dex$. The results of Equation 3.2 are illustrated in Table 3.3 for the four selected stars, together with the stellar mass, expressed in solar masses and the identification number.

At this point, it is necessary to consider the distribution of 1P and 2P stars in the CMD, in particular their separation, to obtain the most reliable estimation of the O variation. Indeed, as we already saw in Section 3.1, the separation between the two populations is not constant and evident along the whole MS but it diminishes moving from the bottom of the MS to the MS knee. To better see this trend, I report the same two histograms in Figure 3.2, highlighting 1P and 2P stars in blue and red respectively in Figure 3.7. From the stellar distribution in the magnitude range just below the MS knee,i.e $20.5 \leq m_{\rm F160W} \leq 22$ shown in the left panel, the separation between 1P and 2P stars is not well defined because the overall stellar density trend has not a clear bi-modality. On the contrary, from stellar distribution at the bottom of the MS, i.e. $22 \leq m_{\rm F160W} \leq 23.5$ shown in the right panel in Figure 3.7, we can clearly see that the separation between the two population is more evident since we can clearly see the two different stellar distributions. This fact implies that in the magnitude range $20.5 \leq m_{\rm F160W} \leq 22.05$, some 1P stars are probably superimposed to 2P stars
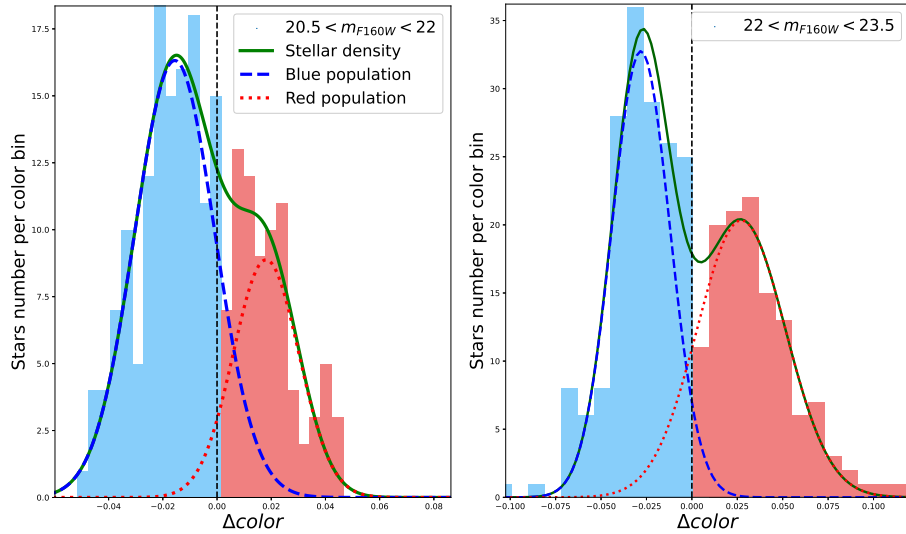
Figure 3.7: Same histograms in Figure 3.2, but 1P and 2P stars are highlighted in blue and red, respectively, to show that the separation between the two populations is much define in the lower part.

in the central regions, therefore in 1P, I am also considering some 2P stars and vice versa. This analysis is also supported by comparing the stellar distribution in Figure 3.7 with the two fiducial lines in Figure 3.3, which are close to each other just below the MS knee and increase their separation moving through fainter stars, and around $m_{\mathrm{F160W}} \sim 21.5 - 22$ they begin to separate sharply.

Considering that the O variation is calculated using the color difference between the two populations , I conclude that the more accurate estimate for the actual O variation between 1P and 2P stars are those derived from the two fainter stars, those with $\Delta O_{1\mathrm{P}-2\mathrm{P}}$ respectively of 0.33 ± 0.03 and 0.32 ± 0.03, due to the wider and better-defined separation between the two populations. Finally, I calculated the weighted mean between these two values obtaining the final result for the O variation:

$$\Delta[O/Fe]_{1\mathrm{P}-2\mathrm{P}} = 0.33 \pm 0.03 \ dex \tag{3.3}$$

This result and its implication for the formation scenarios of MSPs in GCs will be discussed in the last Chapter.

45

Chapter 4

Discussion and conclusion

In this last Chapter, I will discuss the implication of the oxygen variation between 1P and 2P stars inferred from VLM stars in NGC 288 on the formation scenarios of MSPs in GCs. In Section 4.1 I will compare the results about MSPs among VLM stars with results in the literature to support them. In Section 4.2 I will compare the O variation measure between the two populations with that obtained from high-mass stars and I will discuss the implication for the formation scenarios of MSPs in GCs. Finally, in Section 4.2 I will summarize the main results of the present research.

4.1 Multiple populations in NGC 288

In this research, I reduced HST archive data of NGC 288 in optical and NIR with the aim of studying MSPs among VLM stars. Indeed, I identified two distinct stellar populations below the MS knee, in the mass range $\sim 0.5 - 0.1 \ M_\odot$. The NIR CMD with the two stellar populations highlighted in blue and red, representing 1P and 2P stars respectively, are shown in the left panel in Figure 4.2. These stellar populations are also observed in the upper part of the MS, in the SGB (Piotto et al. 2013) and RGB (Jang et al. 2022, hereafter J22). In the upper panels in Figure 4.1, two UV CMDs obtained by Piotto and collaborators using ACS/UVIS are shown to highlight the presence of the two stellar populations. With a zoom-in of the MS, SGB, and RGB, in the bottom panel from the right to the left, respectively, we can recognize clearly these populations that I also detected below the MS knee.

J22 built also the Chromosome map of RGB stars in NGC 288 from ground-based photometry using the B, V and I band, which is displayed in the left panel in Figure 4.2. As already mentioned in Section 1.1, stellar populations with different chemical abundances are located in different regions in the Chromosome map. As we can see, RGB stars are clustered in two main groups of stars, emphasizing the presence of two stellar populations. In particular, stars clustered near the origin are 1P stars and the other 2P stars (for more details about Chromosome Map see Milone et al. 2015).
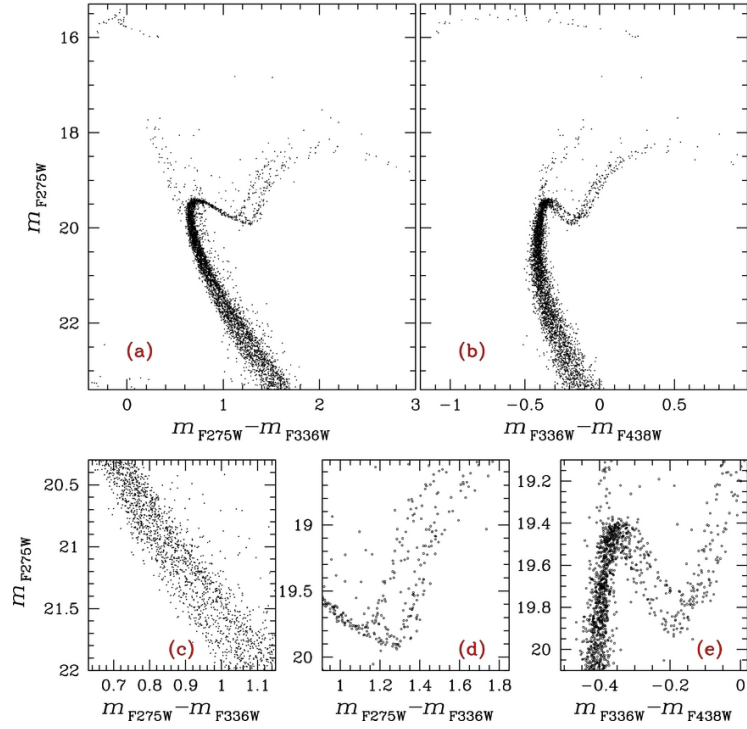
Figure 4.1: *Upper panels*: CMD of NGC 288 from Piotto et al. (2013), which illustrate the upper part of the MS, the SGB, and RGB. *Bottom panels.* Zoom-in of the MS, SGB and RGB to emphasize the presence of two distinct stellar populations. These two stellar populations are those detected also below the MS knee, in this research.
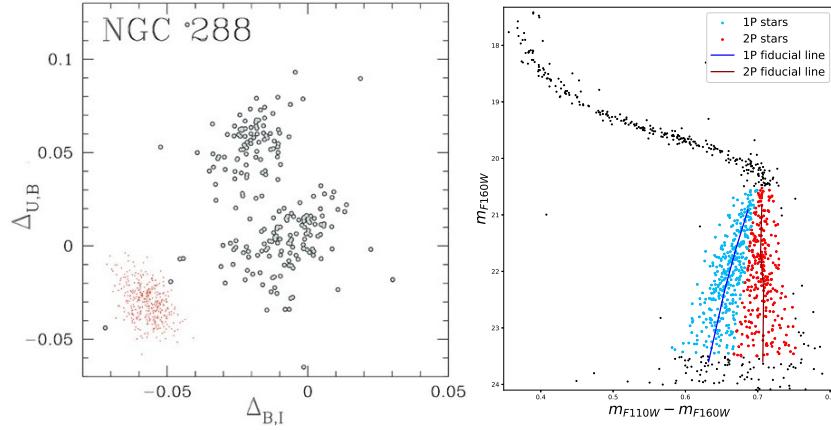

Figure 4.2: *Left panel*:Chromosome map of RGB stars of NGC 288 from J22. *Right panel*: NIR CMD of NGC 288 obtained in this research. 1P and 2P stars with their fiducial line are represented in blue and red, respectively.

Moreover, the bi-modality of the stellar distribution below the MS knee, in particular for $m_{\mathrm{F160W}} \geq 22$, is also observed by Dondoglio et al. (2022).
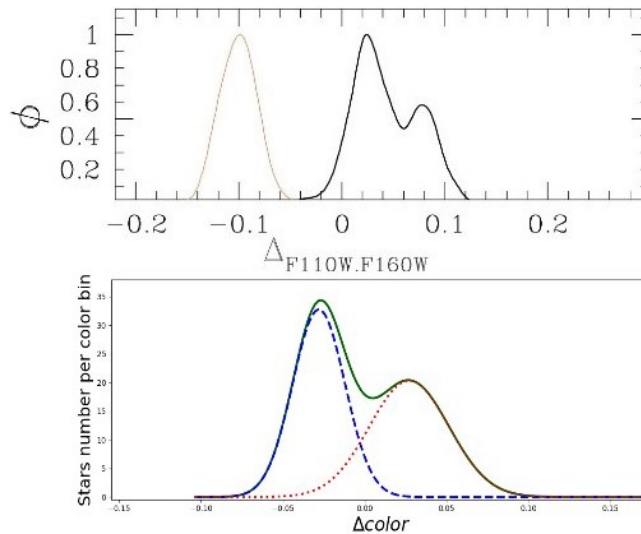
Figure 4.3: Stellar density distribution for stars below the MS knee from Dondoglio et al 2022 (upper panels) and between $22 \leq m_{\text{F160W}} \leq 23.5$ from my research (lower panel). From the comparison, we can see that the distribution that I obtained is compatible with that obtained from Dondoglio and collaborators.

The comparison between the two stellar distributions below the MS knee is displayed in Figure 4.3, where I displayed the result of their work and the stellar distribution below $m_{\text{F160W}} \geq 22$ to better see this bi-modality.

These CMDs, together with the Chromosome Map and the stellar distribution below the MS knee, corroborate the fact that MSPs identified from the RGB down to the upper part of the MS, can also be detected among VLM stars, from the MS knee downward. This result makes it possible to study and characterize this complex and intriguing phenomenon in a new, and largely unexplored, stellar mass range (see Section 1.3.2 for further discussion).

4.2   Oxygen variation in high- and low-mass stars

In this research, I derived for the first time the oxygen variation between 1P and 2P stars among VLM stars in NGC 288, which results in $\Delta O_{1P-2P} = 0.33 \pm 0.03$ dex. I compared my result with literature estimates of the same quantity from Marino et al. (2019) (hereafter Ma19) and J22. These authors inferred the oxygen abundances by means of high-resolution spectroscopy of RGB stars. Their results are listed in Table 4.1. The large oxygen abundance uncertainties from Ma19 are due to the very few spectroscopic targets for which space-based photometry is also available[1]. On the other hand, J22 have many more spectroscopic targets because they used the larger field of view of ground-based photometry, and for this reason, their abundance errors are much smaller. The O variation between 1P a 2P inferred from spectroscopy of RGB stars are provided in Table 4.2. I find that the relative oxygen abundances inferred from

---

[1] Only nine targets had both spectroscopic and space-based photometric measurements, with four targets belonging to 1P stars and five targets belonging to 2P stars.

Population	[O/Fe]
	from Marino et al. 2019
1P	0.25 ± 0.16
2P	0.11 ± 0.26
	from Jang et al. 2022
1P	0.34 ± 0.04
2P	0.06 ± 0.08

Table 4.1: Oxygen abundance derived from high-resolution spectroscopy of 1P and 2P RGB stars (Marino et al. 2019 and Jang et al. 2022).

	$\Delta[O/Fe]_{1P-2P}$
	RGB stars
Marino et al. 2019	0.14 ± 0.30
Jang et al. 2022	0.28 ± 0.09
	VLM stars
This research	0.33 ± 0.03

Table 4.2: O variation between 1P and 2P stars for RGB stars, from Marino et. al 2019 and Jang et al. 2022, and for VLM stars, derived in this research, in NGC 288.

RGB and VLM stars are consistent with each other

The results from my thesis corroborate the conclusion by Dondoglio et al. (2022), who investigated multiple populations among M-dwarfs of nine GCs, including NGC 288. These authors noticed that, below the knee, the MS of this cluster is not consistent with a single isochrone and detected some hints of an MS split.

The conclusion of my thesis are similar to those by M19 on the GC NGC 6752. Milone and collaborators inferred the oxygen variation between 1P and 2P stars below the MS knee by means of NIR photometry and compared this value with results from spectroscopy of RGB. They concluded that the relative oxygen abundances of the multiple populations of NGC 6752 do not depend on stellar mass.

As mentioned in Section 1.3.2, the O difference between 1P and 2P high- and low-mass stars can be used to disentangle the formation scenarios of MSPs in GCs. In particular:

- $\Delta[O/Fe]_{1P-2P}$ **between high- and low-mass stars is comparable**. This result would argue in favor of *Multiple Generations* scenarios considering that we would expect approximately the same O abundance between high- and low-mass stars in the same stellar populations.

- $\Delta[O/Fe]_{1P-2P}$ **between high- and low-mass stars is not comparable**. This would argue instead in favor of *Single Generation* scenarios, since we would expect that the accretion processes during the formation of 2P stars depend on the stellar mass, therefore high- and low-mass should have different chemical abundances.

After these considerations, the result that I obtained is aligned with the scenario predicted by *Multiple Generations* scenarios. However, this result does not rule out the *Single Generation* scenarios but constrains the 2P stars formation processes. In particular, since 2P stars, according to the latter scenario, should form through accretion processes of polluted material produced by 1P stars, these accretion processes should not depend on the 2P stellar mass (e.g. this result excludes Bondi-like accretion processes).

4.3   Summary and Conclusions

In this research, I studied stars located below the MS knee, in NGC 288, in the m_{F160W} versus $m_{\mathrm{F110W}} - m_{\mathrm{F160W}}$ CMD, which are less massive than $\sim$ 0.5 $M_\odot$. This stellar mass range is really poorly explored, with only a few studies dedicated to multiple populations among VLM stars. From the analysis of these stars I found out:

- **Two stellar populations below the MS knee**. I detected two stellar populations below the MS knee, which were detected only by Dondoglio et al. 2022 until now. These two stellar populations are consistent with a first population (1P) and a second population (2P) of stars with different chemical abundances, typical of all GCs. They have also been detected in the upper part of the MS, in the SGB and RGB. This result highlights the importance of VLM stars, which allow the characterization of the MSPs phenomenon in a new, nearly unexplored region of the CMD.

- **Oxygen variation among different stellar populations**. After detecting the two stellar populations, for the first time, I measured the oxygen difference between these stellar populations by comparing the color variation from synthetic spectra with the color difference observed in the NIR CMD. I found a difference of $\Delta[O/Fe]_{\mathrm{1P-2P}} = 0.33 \pm 0.03$ *dex* for VLM stars, which is comparable with the [O/Fe] difference measure for high-mass stars in the RGB. This agreement supports the *Multiple Generations* scenarios because they predict the same chemical abundance in high- and low-mass stars. On the other hand, this result does not rule out *Single Generation* scenarios, but it puts some constraints. In particular, the accretion processes that form 2P stars should not depend on the stellar mass.

Bibliography

J. Anderson, G. Piotto, I. R. King, L. R. Bedin, and P. Guhathakurta. Mixed Populations in Globular Clusters: Et Tu, 47 Tuc? *Astrophysical Journal, Letters*, 697(1):L58–L62, May 2009. doi: 10.1088/0004-637X/697/1/L58.

Jay Anderson and Luigi R. Bedin. An Empirical Pixel-Based Correction for Imperfect CTE. I. HST's Advanced Camera for Surveys. *Publications of the ASP*, 122(895):1035, September 2010. doi: 10.1086/656399.

Jay Anderson and Ivan R. King. Toward High-Precision Astrometry with WFPC2. I. Deriving an Accurate Point-Spread Function. *Publications of the ASP*, 112(776):1360–1382, October 2000. doi: 10.1086/316632.

Jay Anderson, Ivan R. King, Harvey B. Richer, Gregory G. Fahlman, Brad M. S. Hansen, Jarrod Hurley, Jasonjot S. Kalirai, R. Michael Rich, and Peter B. Stetson. Deep Advanced Camera for Surveys Imaging in the Globular Cluster NGC 6397: Reduction Methods. *Astronomical Journal*, 135(6):2114–2128, June 2008a. doi: 10.1088/0004-6256/135/6/2114.

Jay Anderson, Ata Sarajedini, Luigi R. Bedin, Ivan R. King, Giampaolo Piotto, I. Neill Reid, Michael Siegel, Steven R. Majewski, Nathaniel E. Q. Paust, Antonio Aparicio, Antonino P. Milone, Brian Chaboyer, and Alfred Rosenberg. The Acs Survey of Globular Clusters. V. Generating a Comprehensive Star Catalog for each Cluster. *Astronomical Journal*, 135(6):2055–2073, June 2008b. doi: 10.1088/0004-6256/135/6/2055.

I. Baraffe, G. Chabrier, F. Allard, and P. H. Hauschildt. Evolutionary models for metal-poor low-mass stars. Lower main sequence of globular clusters and halo field stars. *Astronomy and Astrophysics*, 327:1054–1069, November 1997.

N. Bastian, H. J. G. L. M. Lamers, S. E. de Mink, S. N. Longmore, S. P. Goodwin, and M. Gieles. Early disc accretion as the origin of abundance anomalies in globular clusters. *Monthly Notices of the RAS*, 436(3):2398–2411, December 2013. doi: 10.1093/mnras/stt1745.

Nate Bastian and Carmela Lardo. Globular cluster mass-loss in the context of multiple populations. *Monthly Notices of the RAS*, 453(1):357–364, October 2015. doi: 10.1093/mnras/stv1661.

Nate Bastian and Carmela Lardo. Multiple Stellar Populations in Globular Clusters. *Annual Review of Astron and Astrophys*, 56:83–136, September 2018. doi: 10.1146/annurev-astro-081817-051839.

H. Baumgardt. N -body modelling of globular clusters: masses, mass-to-light ratios and intermediate-mass black holes. *Monthly Notices of the RAS*, 464 (2):2174–2202, January 2017. doi: 10.1093/mnras/stw2488.

Owen M. Boberg, Jeffrey M. Gerber, Eileen D. Friel, Sarah Martell, Michael M. Briley, and Heather L. Morrison. Limitations of CN and CH Molecular Band Strengths at High Metallicities: A Case Study in NGC 6791. *Astronomical Journal*, 151(5):127, May 2016. doi: 10.3847/0004-6256/151/5/127.

G. Bono, P. B. Stetson, D. A. VandenBerg, A. Calamida, M. Dall'Ora, G. Iannicola, P. Amico, A. Di Cecco, E. Marchetti, M. Monelli, N. Sanna, A. R. Walker, M. Zoccali, R. Buonanno, F. Caputo, C. E. Corsi, S. Degl'Innocenti, S. D'Odorico, I. Ferraro, R. Gilmozzi, J. Melnick, M. Nonino, S. Ortolani, A. M. Piersimoni, P. G. Prada Moroni, L. Pulone, M. Romaniello, and J. Storm. On a New Near-Infrared Method to Estimate the Absolute Ages of Star Clusters: NGC 3201 as a First Test Case. *Astrophysical Journal, Letters*, 708(2):L74–L79, January 2010. doi: 10.1088/2041-8205/708/2/L74.

A. Bragaglia, E. Carretta, R. Gratton, V. D'Orazi, S. Cassisi, and S. Lucatello. Helium in first and second-generation stars in globular clusters from spectroscopy of red giants. *Astronomy and Astrophysics*, 519:A60, September 2010. doi: 10.1051/0004-6361/201014702.

Angela Bragaglia, Christopher Sneden, Eugenio Carretta, Raffaele G. Gratton, Sara Lucatello, Peter F. Bernath, James S. A. Brooke, and Ram S. Ram. Searching for Chemical Signatures of Multiple Stellar Populations in the Old, Massive Open Cluster NGC 6791. *Astrophysical Journal*, 796(1):68, November 2014. doi: 10.1088/0004-637X/796/1/68.

Michael M. Briley, Daniel Harbeck, Graeme H. Smith, and Eva K. Grebel. On the Carbon and Nitrogen Abundances of 47 Tucanae's Main-Sequence Stars. *Astronomical Journal*, 127(3):1588–1593, March 2004. doi: 10.1086/381912.

A. Calamida, G. Bono, P. B. Stetson, L. M. Freyhammer, A. M. Piersimoni, R. Buonanno, F. Caputo, S. Cassisi, M. Castellani, C. E. Corsi, M. Dall'Ora, S. Degl'Innocenti, I. Ferraro, F. Grundahl, M. Hilker, G. Iannicola, M. Monelli, M. Nonino, N. Patat, A. Pietrinferni, P. G. Prada Moroni, F. Primas, L. Pulone, T. Richtler, M. Romaniello, J. Storm, and A. R. Walker. Strömgren Photometry of Galactic Globular Clusters. II. Metallicity Distribution of Red Giants in ω Centauri. *Astrophysical Journal*, 706(2):1277–1298, December 2009. doi: 10.1088/0004-637X/706/2/1277.

E. Carretta, A. Bragaglia, R. G. Gratton, S. Lucatello, G. Catanzaro, F. Leone, M. Bellazzini, R. Claudi, V. D'Orazi, Y. Momany, S. Ortolani, E. Pancino, G. Piotto, A. Recio-Blanco, and E. Sabbi. Na-O anticorrelation and HB. VII. The chemical composition of first and second-generation stars in 15 globular clusters from GIRAFFE spectra. *Astronomy and Astrophysics*, 505(1):117–138, October 2009. doi: 10.1051/0004-6361/200912096.

E. Carretta, A. Bragaglia, R. G. Gratton, S. Lucatello, and V. D'Orazi. Chemical Tagging of Three Distinct Populations of Red Giants in the Globular Cluster NGC 6752. *Astrophysical Journal, Letters*, 750(1):L14, May 2012. doi: 10.1088/2041-8205/750/1/L14.

Eugenio Carretta. Abundances in Red Giant Stars of NGC 2808 and Correlations between Chemical Anomalies and Global Parameters in Globular Clusters. *Astronomical Journal*, 131(3):1766–1783, March 2006. doi: 10.1086/499565.

Eugenio Carretta, Angela Bragaglia, Raffaele Gratton, Sara Lucatello, Michele Bellazzini, and Valentina D'Orazi. Calcium and Light-elements Abundance Variations from High-resolution Spectroscopy in Globular Clusters. *Astrophysical Journal, Letters*, 712(1):L21–L25, March 2010. doi: 10.1088/2041-8205/712/1/L21.

F. Castelli. ATLAS12: how to use it. *Memorie della Societa Astronomica Italiana Supplementi*, 8:25, January 2005.

M. Catelan, F. Grundahl, A. V. Sweigart, A. A. R. Valcarce, and C. Cortés. Constraints on Helium Enhancement in the Globular Cluster M3 (NGC 5272): The Horizontal Branch Test. *Astrophysical Journal, Letters*, 695(1):L97–L102, April 2009. doi: 10.1088/0004-637X/695/1/L97.

J. G. Cohen. Abundances in globular cluster red giants. I. M3 and M13. *Astrophysical Journal*, 223:487–508, July 1978. doi: 10.1086/156284.

Judith G. Cohen, Michael M. Briley, and Peter B. Stetson. Carbon and Nitrogen Abundances in Stars at the Base of the Red Giant Branch in M5. *Astronomical Journal*, 123(5):2525–2540, May 2002. doi: 10.1086/340179.

P. L. Cottrell and G. S. Da Costa. Correlated cyanogen and sodium anomalies in the globular clusters 47 TUC and NGC 6752. *Astrophysical Journal, Letters*, 245:L79–L82, April 1981. doi: 10.1086/183527.

F. Dantona, R. Gratton, and A. Chieffi. CNO self-pollution in globular clusters; a model and its possible observational tests. *Mem. Societa Astronomica Italiana*, 54:173–198, January 1983.

S. E. de Mink, O. R. Pols, N. Langer, and R. G. Izzard. Massive binaries as the source of abundance anomalies in globular clusters. *Astronomy and Astrophysics*, 507(1):L1–L4, November 2009. doi: 10.1051/0004-6361/200913205.

T. Decressin, C. Charbonnel, and G. Meynet. Origin of the abundance patterns in Galactic globular clusters: constraints on dynamical and chemical properties of globular clusters. *Astronomy and Astrophysics*, 475(3):859–873, December 2007a. doi: 10.1051/0004-6361:20078425.

T. Decressin, G. Meynet, C. Charbonnel, N. Prantzos, and S. Ekström. Fast rotating massive stars and the origin of the abundance patterns in galactic globular clusters. *Astronomy and Astrophysics*, 464(3):1029–1044, March 2007b. doi: 10.1051/0004-6361:20066013.

P. A. Denisenkov and S. N. Denisenkova. Correlation Between the Abundances of NA and the CNO Elements in Red Giants in Omega-Centauri. *Soviet Astronomy Letters*, 16:275, July 1990.

Annibale D'Ercole, Francesca D'Antona, Paolo Ventura, Enrico Vesperini, and Stephen L. W. McMillan. Abundance patterns of multiple populations in globular clusters: a chemical evolution model based on yields from AGB ejecta. *Monthly Notices of the RAS*, 407(2):854–869, September 2010. doi: 10.1111/j.1365-2966.2010.16996.x.

E. Dondoglio, A. P. Milone, E. P. Lagioia, A. F. Marino, M. Tailo, G. Cordoni, S. Jang, and M. Carlos. Multiple Stellar Populations along the Red Horizontal Branch and Red Clump of Globular Clusters. *Astrophysical Journal*, 906(2): 76, January 2021. doi: 10.3847/1538-4357/abc882.

E. Dondoglio, A. P. Milone, A. Renzini, E. Vesperini, E. P. Lagioia, A. F. Marino, A. Bellini, M. Carlos, G. Cordoni, S. Jang, M. V. Legnardi, M. Libralato, A. Mohandasan, F. D'Antona, M. Martorano, F. Muratore, and M. Tailo. Survey of Multiple Populations in Globular Clusters among Very-low-mass Stars. *Astrophysical Journal*, 927(2):207, March 2022. doi: 10.3847/1538-4357/ac5046.

Aaron Dotter, Brian Chaboyer, Darko Jevremović, Veselin Kostov, E. Baron, and Jason W. Ferguson. The Dartmouth Stellar Evolution Database. *Astrophysical Journal, Supplement*, 178(1):89–101, September 2008. doi: 10.1086/589654.

Aaron Dotter, Ata Sarajedini, Jay Anderson, Antonio Aparicio, Luigi R. Bedin, Brian Chaboyer, Steven Majewski, A. Marín-Franch, Antonino Milone, Nathaniel Paust, Giampaolo Piotto, I. Neill Reid, Alfred Rosenberg, and Michael Siegel. The ACS Survey of Galactic Globular Clusters. IX. Horizontal Branch Morphology and the Second Parameter Phenomenon. *Astrophysical Journal*, 708(1):698–716, January 2010. doi: 10.1088/0004-637X/708/1/698.

Aaron Dotter, Jason W. Ferguson, Charlie Conroy, A. P. Milone, A. F. Marino, and David Yong. Stellar models of multiple populations in globular clusters - I. The main sequence of NGC 6752. *Monthly Notices of the RAS*, 446(2): 1641–1656, January 2015. doi: 10.1093/mnras/stu2170.

Gaia Collaboration. Gaia Data Release 1. Summary of the astrometric, photometric, and survey properties. *Astronomy and Astrophysics*, 595:A2, November 2016. doi: 10.1051/0004-6361/201629512.

Gaia Collaboration. Gaia Data Release 3: Summary of the content and survey properties. *arXiv e-prints*, art. arXiv:2208.00211, July 2022.

Mark Gieles, Corinne Charbonnel, Martin G. H. Krause, Vincent Hénault-Brunet, Oscar Agertz, Henny J. G. L. M. Lamers, Nathan Bastian, Alessia Gualandris, Alice Zocchi, and James A. Petts. Concurrent formation of supermassive stars and globular clusters: implications for early self-enrichment. *Monthly Notices of the RAS*, 478(2):2461–2479, August 2018. doi: 10.1093/mnras/sty1059.

F. Grundahl, M. Briley, P. E. Nissen, and S. Feltzing. Abundances of RGB stars in NGC 6752. *Astronomy and Astrophysics*, 385:L14–L17, April 2002. doi: 10.1051/0004-6361:20020264.

William E. Harris. A New Catalog of Globular Clusters in the Milky Way. *arXiv e-prints*, art. arXiv:1012.3224, December 2010.

Danny Horta, Ricardo P. Schiavon, J. Ted Mackereth, Timothy C. Beers, José G. Fernández-Trincado, Peter M. Frinchaboy, D. A. García-Hernández, Doug Geisler, Sten Hasselquist, Henrik Jönsson, Richard R. Lane, Steven R. Majewski, Szabolcs Mészáros, Christian Moni Bidin, David M. Nataf, Alexandre Roman-Lopes, Christian Nitschelm, J. Vargas-González, and Gail Zasowski. The chemical compositions of accreted and in situ galactic globular clusters according to SDSS/APOGEE. *Monthly Notices of the RAS*, 493(3):3363–3378, April 2020. doi: 10.1093/mnras/staa478.

S. Jang, A. P. Milone, M. V. Legnardi, A. F. Marino, A. Mastrobuono-Battisti, E. Dondoglio, E. P. Lagioia, L. Casagrande, M. Carlos, A. Mohandasan, G. Cordoni, E. Bortolan, and Y. W. Lee. Chromosome maps of globular clusters from wide-field ground-based photometry. *Monthly Notices of the RAS*, 517(4):5687–5703, December 2022. doi: 10.1093/mnras/stac3086.

Bülent Kızıltan, Holger Baumgardt, and Abraham Loeb. An intermediate-mass black hole in the centre of the globular cluster 47 Tucanae. *Nature*, 542(7640): 203–205, February 2017. doi: 10.1038/nature21361.

Robert P. Kraft. Abundance Differences among Globular Cluster Giants: Primordial vs. Evolutionary Scenarios. *Publications of the ASP*, 106:553, June 1994. doi: 10.1086/133416.

Robert L. Kurucz. *SYNTHE spectrum synthesis programs and line data.* 1993.

Robert L. Kurucz. ATLAS12, SYNTHE, ATLAS9, WIDTH9, et cetera. *Memorie della Societa Astronomica Italiana Supplementi*, 8:14, January 2005.

Robert L. Kurucz and Eugene H. Avrett. Solar Spectrum Synthesis. I. A Sample Atlas from 224 to 300 nm. *SAO Special Report*, 391, May 1981.

E. P. Lagioia, A. P. Milone, A. F. Marino, M. Tailo, A. Renzini, M. Carlos, G. Cordoni, E. Dondoglio, S. Jang, A. Karakas, and A. Dotter. Multiple Stellar Populations in Asymptotic Giant Branch Stars of Galactic Globular Clusters. *Astrophysical Journal*, 910(1):6, March 2021. doi: 10.3847/1538-4357/abdfcf.

Edoardo P. Lagioia, Antonino P. Milone, Anna F. Marino, and Aaron Dotter. Helium Variation in Four Small Magellanic Cloud Globular Clusters. *Astrophysical Journal*, 871(2):140, February 2019. doi: 10.3847/1538-4357/aaf729.

C. Loup, T. Forveille, A. Omont, and J. F. Paul. CO and HCN observations of circumstellar envelopes. A catalogue - mass loss rates and distributions. *Astronomy and Astrophysicss*, 99:291–377, June 1993.

Piero Madau and Mark Dickinson. Cosmic Star-Formation History. *Annual Review of Astron and Astrophys*, 52:415–486, August 2014. doi: 10.1146/annurev-astro-081811-125615.

A. F. Marino, A. P. Milone, D. Yong, G. Da Costa, M. Asplund, L. R. Bedin, H. Jerjen, D. Nardiello, G. Piotto, A. Renzini, and M. Shetrone. Spectroscopy and Photometry of Multiple Populations along the Asymptotic Giant Branch of NGC 2808 and NGC 6121 (M4). *Astrophysical Journal*, 843(1):66, July 2017. doi: 10.3847/1538-4357/aa7852.

A. F. Marino, A. P. Milone, A. Renzini, F. D'Antona, J. Anderson, L. R. Bedin, A. Bellini, G. Cordoni, E. P. Lagioia, G. Piotto, and M. Tailo. The Hubble Space Telescope UV Legacy Survey of Galactic Globular Clusters - XIX. A chemical tagging of the multiple stellar populations over the chromosome maps. *Monthly Notices of the RAS*, 487(3):3815–3844, August 2019. doi: 10.1093/mnras/stz1415.

Marino, A. F., Villanova, S., Piotto, G., Milone, A. P., Momany, Y., Bedin, L. R., and Medling, A. M. Spectroscopic and photometric evidence of two stellar populations in the galactic globular cluster ngc 6121 (m***. *A&A*, 490(2): 625–640, 2008. doi: 10.1051/0004-6361:200810389. URL https://doi.org/10.1051/0004-6361:200810389.

A. P. Milone, A. F. Marino, S. Cassisi, G. Piotto, L. R. Bedin, J. Anderson, F. Allard, A. Aparicio, A. Bellini, R. Buonanno, M. Monelli, and A. Pietrinferni. The Infrared Eye of the Wide-Field Camera 3 on the Hubble Space Telescope Reveals Multiple Main Sequences of Very Low Mass Stars in NGC 2808. *Astrophysical Journal, Letters*, 2012a.

A. P. Milone, A. F. Marino, G. Piotto, L. R. Bedin, J. Anderson, A. Aparicio, S. Cassisi, and R. M. Rich. A Double Main Sequence in the Globular Cluster NGC 6397. *Astrophysical Journal*, 2012b.

A. P. Milone, G. Piotto, L. R. Bedin, A. Aparicio, J. Anderson, A. Sarajedini, A. F. Marino, A. Moretti, M. B. Davies, B. Chaboyer, A. Dotter, M. Hempel, A. Marín-Franch, S. Majewski, N. E. Q. Paust, I. N. Reid, A. Rosenberg, and M. Siegel. The ACS survey of Galactic globular clusters. XII. Photometric binaries along the main sequence. *Astronomy and Astrophysics*, 540:A16, April 2012c. doi: 10.1051/0004-6361/201016384.

A. P. Milone, G. Piotto, L. R. Bedin, I. R. King, J. Anderson, A. F. Marino, A. Bellini, R. Gratton, A. Renzini, P. B. Stetson, S. Cassisi, A. Aparicio, A. Bragaglia, E. Carretta, F. D'Antona, M. Di Criscienzo, S. Lucatello, M. Monelli, and A. Pietrinferni. Multiple Stellar Populations in 47 Tucanae. *Astrophysical Journal*, 2012d.

A. P. Milone, A. F. Marino, L. R. Bedin, G. Piotto, S. Cassisi, A. Dieball, J. Anderson, H. Jerjen, M. Asplund, A. Bellini, K. Brogaard, A. Dotter, M. Giersz, D. C. Heggie, C. Knigge, R. M. Rich, M. van den Berg, and R. Buonanno. The M 4 Core Project with HST - II. Multiple stellar populations at the bottom of the main sequence. *Monthly Notices of the RAS*, 439(2):1588–1595, April 2014. doi: 10.1093/mnras/stu030.

A. P. Milone, A. F. Marino, L. R. Bedin, J. Anderson, D. Apai, A. Bellini, P. Bergeron, A. J. Burgasser, A. Dotter, and J. M. Rees. The HST large programme on ω Centauri - I. Multiple stellar populations at the bottom of

the main sequence probed in NIR-Optical. *Monthly Notices of the RAS*, 469 (1):800–812, July 2017a. doi: 10.1093/mnras/stx836.

A. P. Milone, G. Piotto, A. Renzini, A. F. Marino, L. R. Bedin, E. Vesperini, F. D'Antona, D. Nardiello, J. Anderson, I. R. King, D. Yong, A. Bellini, A. Aparicio, B. Barbuy, T. M. Brown, S. Cassisi, S. Ortolani, M. Salaris, A. Sarajedini, and R. P. van der Marel. The Hubble Space Telescope UV Legacy Survey of Galactic globular clusters - IX. The Atlas of multiple stellar populations. *Monthly Notices of the RAS*, 464(3):3636–3656, January 2017b. doi: 10.1093/mnras/stw2531.

A. P. Milone, A. F. Marino, A. Renzini, F. D'Antona, J. Anderson, B. Barbuy, L. R. Bedin, A. Bellini, T. M. Brown, S. Cassisi, G. Cordoni, E. P. Lagioia, D. Nardiello, S. Ortolani, G. Piotto, A. Sarajedini, M. Tailo, R. P. van der Marel, and E. Vesperini. The Hubble Space Telescope UV legacy survey of galactic globular clusters - XVI. The helium abundance of multiple populations. *Monthly Notices of the RAS*, 481(4):5098–5122, December 2018. doi: 10.1093/mnras/sty2573.

A. P. Milone, A. F. Marino, L. R. Bedin, J. Anderson, D. Apai, A. Bellini, A. Dieball, M. Salaris, M. Libralato, D. Nardiello, P. Bergeron, A. J. Burgasser, J. M. Rees, R. M. Rich, and H. B. Richer. The HST Large Programme on NGC 6752 - II. Multiple populations at the bottom of the main sequence probed in NIR. *Monthly Notices of the RAS*, 484(3):4046–4053, April 2019. doi: 10.1093/mnras/stz277.

D. Nardiello, A. P. Milone, G. Piotto, A. F. Marino, A. Bellini, and S. Cassisi. Observing multiple stellar populations with VLT/FORS2. Main sequence photometry in outer regions of NGC 6752, NGC 6397, and NGC 6121 (M 4). *Astronomy and Astrophysics*, 573:A70, January 2015. doi: 10.1051/0004-6361/201424117.

J. Norris and K. C. Freeman. The anticorrelation of carbon and nitrogen on the horizontal branch of 47 Tuc. *Astrophysical Journal*, 254:143, March 1982. doi: 10.1086/159717.

J. Norris, P. L. Cottrell, K. C. Freeman, and G. S. Da Costa. The abundance spread in the giants of NGC 6752. *Astrophysical Journal*, 244:205–220, February 1981. doi: 10.1086/158698.

G. Piotto, A. P. Milone, A. F. Marino, L. R. Bedin, J. Anderson, H. Jerjen, A. Bellini, and S. Cassisi. Multi-wavelength Hubble Space Telescope Photometry of Stellar Populations in NGC 288. *Astrophysical Journal*, 775(1): 15, September 2013. doi: 10.1088/0004-637X/775/1/15.

Giampaolo Piotto. Observational Evidence of Multiple Stellar Populations in Globular Clusters. In Enrico Vesperini, Mirek Giersz, and Alison Sills, editors, *Dynamical Evolution of Dense Stellar Systems*, volume 246, pages 141–150, May 2008. doi: 10.1017/S1743921308015482.

S. F. Portegies Zwart, J. Makino, S. L. W. McMillan, and P. Hut. Star cluster ecology. III. Runaway collisions in young compact star clusters. *Astronomy and Astrophysics*, 348:117–126, August 1999.

A. Renzini, F. D'Antona, S. Cassisi, I. R. King, A. P. Milone, P. Ventura, J. Anderson, L. R. Bedin, A. Bellini, T. M. Brown, G. Piotto, R. P. van der Marel, B. Barbuy, E. Dalessandro, S. Hidalgo, A. F. Marino, S. Ortolani, M. Salaris, and A. Sarajedini. The Hubble Space Telescope UV Legacy Survey of Galactic Globular Clusters - V. Constraints on formation scenarios. *Monthly Notices of the RAS*, 454(4):4197–4207, December 2015. doi: 10.1093/mnras/stv2268.

Alvio Renzini. Rethinking globular clusters formation. *Mem. Societa Astronomica Italiana*, 84:162, January 2013.

Joel C. Roediger, Stéphane Courteau, Genevieve Graves, and Ricardo P. Schiavon. Constraining Stellar Population Models. I. Age, Metallicity and Abundance Pattern Compilation for Galactic Globular Clusters. *Astrophysical Journal, Supplement*, 210(1):10, January 2014. doi: 10.1088/0067-0049/210/1/10.

Allan Sandage and Robert Wildey. The Anomalous Color-Magnitude Diagram of the Remote Globular Cluster NGC 7006. *Astrophysical Journal*, 150:469, November 1967. doi: 10.1086/149350.

Graeme H. Smith and Alan J. Penny. CN and CH Inhomogeneities among Red Horizontal Branch Stars in M71. *Astronomical Journal*, 97:1397, May 1989. doi: 10.1086/115080.

Paolo Ventura, Francesca D'Antona, Italo Mazzitelli, and Raffaele Gratton. Predictions for Self-Pollution in Globular Cluster Stars. *Astrophysical Journal, Letters*, 550(1):L65–L69, March 2001. doi: 10.1086/319496.

Enrico Vesperini, Stephen L. W. McMillan, Francesca D'Antona, and Annibale D'Ercole. The Fraction of Globular Cluster Second-generation Stars in the Galactic Halo. *Astrophysical Journal, Letters*, 718(2):L112–L116, August 2010. doi: 10.1088/2041-8205/718/2/L112.

D. Yong, F. Grundahl, D. L. Lambert, P. E. Nissen, and M. D. Shetrone. Mg isotopic ratios in giant stars of the globular cluster NGC 6752. *Astronomy and Astrophysics*, 402:985–1001, May 2003. doi: 10.1051/0004-6361:20030296.

David Yong, Frank Grundahl, Jennifer A. Johnson, and Martin Asplund. Nitrogen Abundances in Giant Stars of the Globular Cluster NGC 6752. *Astrophysical Journal*, 684(2):1159–1169, September 2008. doi: 10.1086/590658.

M. Zennaro, A. P. Milone, A. F. Marino, G. Cordoni, E. P. Lagioia, and M. Tailo. Four stellar populations and extreme helium variation in the massive outerhalo globular cluster NGC 2419. *Monthly Notices of the RAS*, 487(3):3239–3251, August 2019. doi: 10.1093/mnras/stz1477.